OPEN ACCESS

KING'S College LONDON

King's Research Portal

DOI:
10.1016/j.jmps.2018.08.004

Document Version
Peer reviewed version

Link to publication record in King's Research Portal

Citation for published version (APA):
Barzdajn, B., Paxton, A. T., Stewart, D., & Dunne, F. P. E. (2018). A Crystal Plasticity Assessment of Normally-loaded Sliding Contact in Rough Surfaces and Galling. *JOURNAL OF THE MECHANICS AND PHYSICS OF SOLIDS*, *121*, 517-542. https://doi.org/10.1016/j.jmps.2018.08.004

Citing this paper
Please note that where the full-text provided on King's Research Portal is the Author Accepted Manuscript or Post-Print version this may differ from the final Published version. If citing, it is advised that you check and use the publisher's definitive version for pagination, volume/issue, and date of publication details. And where the final published version is provided on the Research Portal, if citing you are again advised to check the publisher's website for any subsequent corrections.

General rights
Copyright and moral rights for the publications made accessible in the Research Portal are retained by the authors and/or other copyright owners and it is a condition of accessing publications that users recognize and abide by the legal requirements associated with these rights.

•Users may download and print one copy of any publication from the Research Portal for the purpose of private study or research.
•You may not further distribute the material or use it for any profit-making activity or commercial gain
•You may freely distribute the URL identifying the publication in the Research Portal

Take down policy
If you believe that this document breaches copyright please contact librarypure@kcl.ac.uk providing details, and we will remove access to the work immediately and investigate your claim.

Download date: 04. May. 2023

Accepted Manuscript

A Crystal Plasticity Assessment of Normally-loaded Sliding Contact in Rough Surfaces and Galling

Bartosz Barzdajn , Anthony T. Paxton , David Stewart , Fionn P.E. Dunne

PII: S0022-5096(18)30304-1
DOI: https://doi.org/10.1016/j.jmps.2018.08.004
Reference: MPS 3409

To appear in: *Journal of the Mechanics and Physics of Solids*

Received date: 25 April 2018
Revised date: 24 July 2018
Accepted date: 10 August 2018

Please cite this article as: Bartosz Barzdajn , Anthony T. Paxton , David Stewart , Fionn P.E. Dunne , A Crystal Plasticity Assessment of Normally-loaded Sliding Contact in Rough Surfaces and Galling, *Journal of the Mechanics and Physics of Solids* (2018), doi: https://doi.org/10.1016/j.jmps.2018.08.004

This is a PDF file of an unedited manuscript that has been accepted for publication. As a service to our customers we are providing this early version of the manuscript. The manuscript will undergo copyediting, typesetting, and review of the resulting proof before it is published in its final form. Please note that during the production process errors may be discovered which could affect the content, and all legal disclaimers that apply to the journal pertain.

ACCEPTED MANUSCRIPT

A Crystal Plasticity Assessment of Normally-loaded Sliding Contact in Rough Surfaces and Galling

Bartosz Barzdajn[a,1,*], Anthony T. Paxton[b], David Stewart[c], Fionn P.E. Dunne[a]

[a]Department of Materials, Imperial College, London SW67 2AZ, UK

[b]Department of Physics, King's College London, London WC2R 2LS, UK

[c]Rolls-Royce plc, Raynesway, Derby DE21, UK

[1]Now at School of Materials, The University of Manchester, Manchester M13 9PL, UK

Abstract

An investigation of rough metal to metal contacting surfaces under normal load and undergoing sliding has been carried out with explicit representation of measured surface profiles within a crystal plasticity finite element formulation in which grain size, texture and slip properties are incorporated. A new metric called plastic reach has been introduced for contacting surfaces which reflects both the magnitude of the local surface asperity plasticity and its spatial reach. This quantity has been shown to obey a power law relationship with the applied normal load for sliding contact which in turn has been related to a hazard function. In this way, a new methodology to predict the galling frequency that follows a Weibull distribution has been established. Additionally, a quantitative definition of galling for the class of metal on metal contacting surfaces is considered. The predicted galling frequency distribution for a 316 stainless steel has been compared with independently experimentally measured galling frequencies showing qualitative agreement of the distributions. An assessment of confidence limits has also therefore been provided for the modelling methodology.

ACCEPTED MANUSCRIPT

Keywords: galling, rough surfaces, sliding contact, crystal plasticity

* Corresponding author: *bartosz.barzdajn@manchester.ac.uk*

1. Introduction

This paper addresses the problem of galling of metallic materials. The ASTM G98 - 02 standard defines galling as a form of surface damage arising between sliding solids, distinguished by macroscopic, usually localised, roughening and creation of protrusions above the original surface; it often includes plastic flow or material transfer, or both. At best, the definitions of galling in usage remain highly qualitative. Galling occurs under poor lubrication, at high temperatures and high contact stresses and is an important consideration in engines, pumps and valves since at worst, it can result in seizure, which is the least desired and potentially dangerous outcome.

Hard-facing alloys have been developed, particularly in the nuclear industry, to resist galling. Cobalt-based alloys possess excellent galling properties (Antony, 1983) but a significant disadvantage in pressurised water reactors is that coolant from the primary circuit is exposed to significant neutron radiation. The wear debris which contains cobalt, released during operation of valves and pumps, undergoes a transition to $^{60}_{27}\mathrm{Co}$. This isotope is a strong emitter of dangerous gamma radiation with a long half-life of about 5 years, potentially giving rise to human exposure (Ocken, 1985). Hence industrial users and researchers have sought to eliminate cobalt from hard-facing alloys in nuclear application. Alternative alloys under consideration include chromium rich, austenitic or duplex stainless steels (Davis, 1994).

Metal surfaces are rough and have complex morphology, and when nominally flat surfaces are brought together, the true area of contact is only a fraction of the apparent area. Contact comprises the collective individual interactions of asperities. As a result, wear is a multiscale and complex problem in which sliding surface deformation is associated with large stresses, concentrated near contact spots and significant localised plastic straining. For typically finished hard-facings (arithmetical mean roughness value $R_a \approx 10^{-1}\ \mu$m) the individual contact spots, as well as the related plastic zones, are on the scale of micrometers. Furthermore, the formation of wear particles depends on the work necessary to form new surfaces and on the existing local stored energy. Local shearing and pull-out forces depend on traction between surfaces in contact but also on the nature of the bonding at the contact spots. For example, when an oxide layer is present, the dominant bonding type could be van der Waals. Once this layer is removed the bonding may become metallic.

Rabinowicz (1973) addressed interfacial seizure which may be accompanied by gross surface welding (Gee, 1969) and suggested that galling seizure is the result of excessive normal load, accompanied by severe surface damage. Galling seizure was argued to occur when wear particle size becomes greater than the clearance between contacting rough surfaces. In earlier work, the key quantity defining wear rate was taken to be the work of adhesion W_{ab}

$$W_{ab} = \gamma_a + \gamma_b - \gamma_{ab},$$

where γ_a and γ_b are the surface energies of materials a and b respectively, while γ_{ab} is the interface free energy (Rabinowicz 1961) which led to galling resistance being related to resistance to wear. However, Hsu *et al.* (1980) found that free machining alloys have poor wear rate, but high galling resistance. Nitronic 60, an austenitic steel, also had high wear rate in comparison to other austenitic steels, while being galling resistant so that the relation between wear and galling resistance is not straightforward.

An additional mechanistic process potentially occurring under high normal interfacial stress is phase change. In 304 stainless steel, high strains near the interface introduce phase transformation from austenite to much harder $\alpha'-$ martensite (bct). Such a state may result in pushing the plastic deformation deeper into the bulk, generating strong hardness gradients. A correlation between gradients of hardness and galling tendency has been reported (Hsu *et al.*, 1980; Vinogradov, 1957), but it is noted that strain or stress assisted phase transformation depends also on stacking fault energies (SFEs) (Olson *et al.,* 1976). That is, the SFE is important in both hardening and phase transformation and hence the role of SFE in galling remains ambiguous. The significance of strain induced phase transformation in galling was also supported by Yang *et al.* (1985).

Adhesion between contacting metal surfaces is clearly important in seizure, as pointed out by Boas *et al.,* (1977), who also recognized galling as a stochastic phenomenon in which the threshold normal load was associated with the fraction of tests which resulted in seizure. Budinski (1981) defines incipient galling as the early stages of surface deformation and adhesion in metal-to-metal wear, but in the absence of seizure. Galling resistance was argued to relate to plasticity and the ratio of tensile strength to yield strength, with a value near unity giving poor galling resistance. In accordance with some previous observations, harder materials tended to gall less. The morphology of the contacting interfaces was found to be significant for the galling resistance; surface waviness and error of form resulted in significant impact on galling. Morphology determines the number and nature of asperity contacts which have to carry the same applied loading; a smaller number of asperities results in greater local deformation. Budinski also noted that highly polished surfaces ($\sim 0.25\ \mu$m) gave highest galling tendencies, while abrasively blasted surfaces ($\sim 1\ \mu$m) behaved with better galling response. In contrast, electropolishing, which leads to reduction of roughness, has been argued to give positive effects on galling performance (Able Electropolishing, 2017; Delstar Metal Finishing, 2017). Vikström (1994) also found an influence of profile morphology on galling; highly polished surfaces ($R_a < 0.25\ \mu$m) were incapable of storing wear particles, while very rough finishes $R_a > 1.50\ \mu$m resulted in interlocking of

asperities. The apparent contradictions imply that surface roughness in its own right is not necessarily indicative of galling performance, but that other characteristics of the surface profile (*e.g.* asperity curvature, average spacing *etc*.) are potentially important. This view was suggested by Podgornik *et al.* (2012) and reinforced by empirical evidence.

The role of SFE in galling was assessed by Bhansali and Miller (1982). Contrary to Rabinowicz (1961), they associated galling with an increase of wear particle size and emphasised the role of plastic deformation, arguing that hardness was not a good indicator of wear or galling performance. The work supported the mechanistic arguments of Kragelsky and Aleksev (1976) such that severe asperity plastic deformation occurs and accumulates ahead of moving asperities, effectively forged in to the interfacial spaces. A consequence is increase in true area of contact, asperity interlocking, and severity of plastic deformation, in keeping with Budinski (1981). Bhansali *et al.* conclude that low stacking fault energy prevents cross-slip, limits mobility of dislocations and plastic deformation, while enhancing hardening rate. As a result the asperities in contact prefer to fracture rather than deform, requiring less energy and resulting in better galling resistance. Cobalt, nickel and iron based alloys with known stacking fault densities measured using X-ray diffraction indicate that lower SFEs apparently lead to better galling resistance but it remains unclear whether this results from hardening or surface phase transformation (or both). The importance of strain induced transformation is also assessed by Ohriner *et al*. (1991) who conclude on the basis of work by Schumacher (1981) and Hsu *et al.* (1980) and in accordance with Bhansali *et al.* (1982), that good galling resistance is associated with low SFEs since they favour strain induced phase transformation to much harder products.

The role of fracture in galling resistant materials is discussed by Ocken (1995), who considers the potentially positive influence of carbides; the beneficial role of these phases was confirmed by Cockeram *et al.* (1997) who found that the brittle phases provided resistance to surface damage during contact sliding. Subsequently, Cockeram (2002) investigated the influence of δ-ferrite content on hardness, galling resistance, and fracture toughness in iron-based alloys; galling resistance improved with the increasing fraction of the δ-ferrite. Cockeram argued that more phase boundaries promoted stress induced phase transformation to martensite resulting in better galling performance.

Kim *et al.* (2000; 2001) studied temperature effects on galling in iron-based austenitic NOREM 02, designed to have low stacking fault energy. This alloy at 20°C gives excellent tribological properties, but at temperature greater than 180°C, galling occurred. Microhardness measurements beneath the worn surface revealed that at temperatures above 180°C, there was a significant decrease in hardness. Hence it was suggested that the sudden drop in performance was mainly due to the loss of work hardening. Analysis of the worn surface tested above 190°C also showed the absence of α' – martensite (bct). The transformation was considered beneficial to galling, and it was concluded that the transition occurred between 180-190°C and that it was responsible for the change from mild to severe wear.

It is apparent from the above that galling is complex and a range of factors have been established which are potentially important. These include adhesion and plasticity; the propensity of the material to harden, or to undergo phase transformations leading to harder products, both depending on SFE. Surface morphologies also are argued to be key, both in terms of roughness and more detailed characteristics including asperity geometries and spacing. Further, hard-phase particles and the establishment of corrosion layers are known to be relevant. This paper aims to provide a complementary approach to those presented above in understanding galling. The methodology is to simplify, in order to examine the role of a subset of those factors deemed important above. This is done by the establishment of geometrically representative polycrystal models of contacting nominally flat (but rough) surfaces. In this way, crystal slip (taking due account of the considerable elastic and plastic anisotropies) at contacting surfaces, and in particular at the key contacting asperities, in normally-loaded sliding contact may be assessed. Full account is taken of the surface profiles (obtained from profilometry measurements), the grain size, texture and geometric properties of the contacting rough surfaces (*e.g.* roughness and wavelength), as well as the underlying material properties of intrinsic slip strength and hardening (thereby representing stacking fault energy). Through consideration of slip localization and its sub-surface reach, a new quantitative definition of galling is introduced and tested against experimental galling data in the literature. The model provides a methodology by which some of the experimental observations described above may be tested; in particular, the role of surface profile, crystal properties and microstructure.

2. Methodology

We recognize the stochastic nature of galling experiments for which there is clear agreement in the literature and as a result, we firstly introduce the methodology required to represent the statistics of galling and the interpretation of the experimental data available. At the same time we acknowledge that underlying mechanisms are in fact deterministic. Nonetheless, this leads to the description of a finite element model representation of a measured rough surface utilizing continuum plasticity, and subjected to normally-loaded, frictional sliding contact in order to gain insight in to the appropriate length scale at which the local plastic deformation occurs. This provides an assessment of the key microstructural features likely to be important, with respect to the length scale set by the surface profile geometry. Because it transpires that this length scale is of the order of the grain size (for the quantified surface profile and material considered), a crystal plasticity modelling approach is found to be necessary and this is then outlined. This is followed by the establishment of a representative galling model for which it is

necessary to define surface profile geometry, polycrystal morphology and texture followed by contact, boundary and loading conditions. This then leads in to the description of the investigations carried out and the results obtained.

2.1. Stochastic interpretation of galling experiments

Galling resistance is commonly ranked using ASTM G98 Standard Test Method for Galling Resistance of Material Couples and the related ASTM G196. The principles of the measurement set-up are very similar in both cases. Two cylindrical specimens with nominally flat surfaces are brought into contact under constant normal load. Then, one of the specimens is forced to rotate one full revolution. Subsequently, specimens are visually investigated for any signs of galling. If none of them is galled, the procedure is repeated with increased normal load. The normal pressure under which samples start to show damage is reported as the galling threshold pressure of the sample. In the newer ASTM G196 standard, hollow cylinders are used, resulting in more uniform stress distribution across the contact interface and more uniform sliding speed (Waite *et al.*, 2006; Hummel, 2008). However, more importantly, ASTM G196 recognises galling as a stochastic phenomenon. As reported in (Hummel, 2008; Hummel *et al.* 2009), very similar samples, machined from the same batch of the material, gall at different normal loads. Hence, instead of reporting a single galling threshold pressure as a characteristic of a material couple, the normal pressure at which 50% of samples have galled is used, referred to as the galling_{50} stochastic measure of galling (Hummel *et al.*, 2009). This quantity is derived from a series of experiments. Multiple samples are tested respectively under several normal loads. For each value of normal load, the fraction of samples which gall is evaluated. This fraction serves as an estimate of galling probability. The probability of galling versus normal load so obtained generates a sigmoidal variation from which the galling_{50} measure is evaluated. The details of the probabilistic formulation are given in Appendix A, but in summary, the probability of failure $F(l)$ as a function of normal load l, may be written in terms of a cumulative hazard function, $H(l)$, whose properties are useful in the context of representing the characteristics of the contacting, loaded surfaces to be presented later

$$F(l) = 1 - e^{-H(l)}. \tag{1}$$

Hence if the hazard function can be related to key quantities which are found to be characteristic of galling, and accessible from the crystal plasticity model of the normally-loaded contacting sliding surfaces, then so the probability distribution for galling failure may be established. In this way, a capability for predicting galling failure distributions potentially becomes possible. However, the crystal plasticity geometric model must be representative in terms of microstructure (number of grains, morphology and crystallography) and surface profile (number of represented asperities, their spatial distribution, height, radius), and these requirements need to be met in order for the above relationship between galling failure distribution and hazard function to be useful. More detailed consideration of what is needed for chosen microstructures and surface profiles to be representative is given in Appendices B and C.

2.2. Contacting surfaces: geometry, boundary conditions and scale

Contacting surfaces even under considerable normal loading in fact interact over a small fraction of the apparent contact area as a result of surface roughness, the scale and magnitude of which is often determined by the prior surface treatment. Hence the matter of choosing the appropriate length scale over which to establish appropriate studies to investigate sliding contact and galling is important. We start from consideration of the galling standard ASTM G196 for which a representation of the standard test is depicted in in figure 1(a).

ACCEPTED MANUSCRIPT

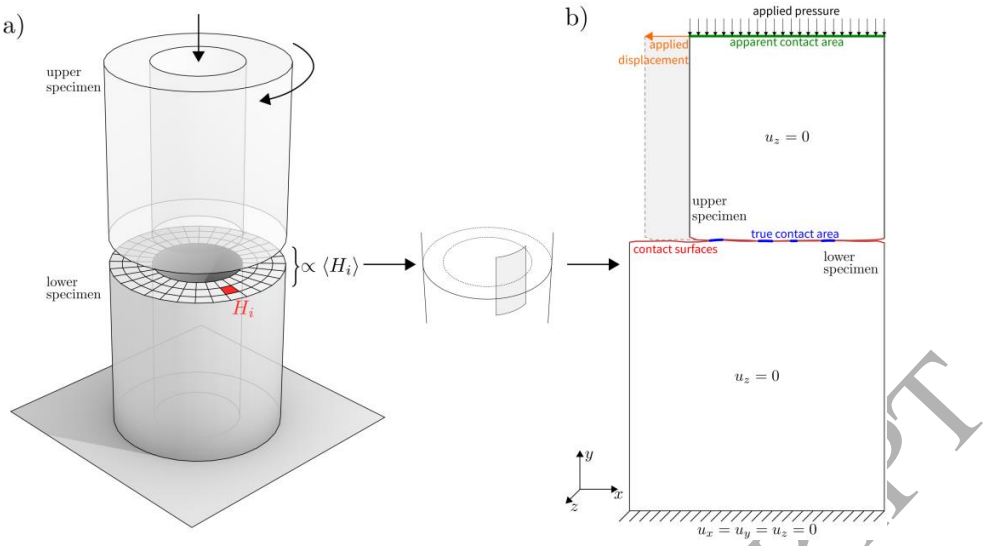

Figure 1. Geometry of (a) the standard galling test set-up and (b) schematic view of the "in-plane" subdivision of the contact interface illustrating proposed geometry and boundary conditions for the finite element model.

However, the length scale associated with the surface roughness (of order μm) is orders of magnitude smaller than that associated with the radius (mm) of the cylindrical test sample in Figure 1(a). As a consequence, it is reasonable to consider a much smaller representative geometry for the contact zone which is planar, since the cylinder curvature at this length scale is negligible. This is shown schematically in Figure 1(b) together with the chosen boundary conditions. The upper specimen is in sliding contact with the lower part and subjected to the normal loading pressure which is transmitted through the true contact areas to the lower specimen. For reasons of computational efficiency, while the model is three dimensional, conditions of plane strain are imposed (z-displacements on the front and back faces are constrained to be zero). Once the normal (y-direction) pressure loading has been imposed, the upper specimen is displaced in the (negative) x-direction to cause sliding contact of the rough surfaces. The latter, shown schematically in Figure 1(b) are in fact chosen to replicate profilometric measurements of the surface of the iron-based hard-facing material RR2450. These are shown in Figure 2 and are represented in the geometric modelling using cubic splines.

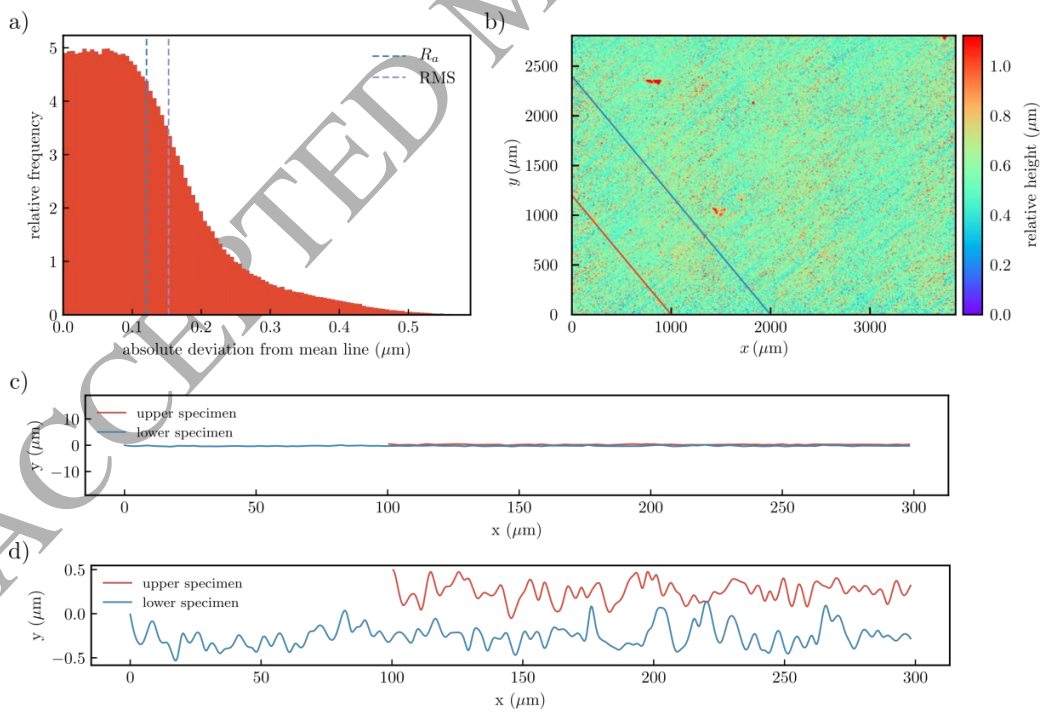

Figure 2. (a) Frequency distribution of relative height and (b) surface map of alloy RR2450. The red and blue lines represent the profiles taken to create the contact surfaces of the upper and lower specimens respectively. The in-plane resolution of the measurements (sampling distance in subfigure (b)) is 2.76 μm. Mean roughness R_a = 0.12 μm, RMS roughness= 0.15 μm. The resulting two profiles (linear sub-sets taken from (a)) are shown in (c) and (d) with the scales shown. Courtesy of Dr David Bowden (The University of Manchester).

The resulting model representation of the upper (200 × 200 × 0.2 μm) and lower (300 × 300 × 0.2 μm) specimens is shown in Figure 3(a) where the rough contacting surfaces may be seen at the interface. A finite element modelling approach is adopted and the meshing can also be seen in the figure, showing considerable refinement at the regions of contact (typical element dimension being 0.2 μm). Quadratic, 3D 20-noded brick elements (C3D20R) are utilized within the FE software ABAQUS. Microstructural representation is not yet incorporated (but see later) since the primary initial objective is to understand the length scale of the deformation fields which result as a consequence of the geometry of the rough contacting surfaces. The contact definition selected is that provided within the ABAQUS software in which a "hard" pressure-overclosure relationship is utilised, such that penetration of the master surface by the slave surface is minimised and there is no transfer of tensile stress. This incorporates a linear penalty method, with penalty stiffness ten times greater than the effective stiffness of the underlying elements. This method, together with that of Lagrange multipliers and the augmented Lagrangian approach, is in common usage (Weyler *et. al.*, 2012). Contrary to Lagrange multipliers, the penalty method does not introduce additional equilibrium iterations, which was chosen to minimise additional complexity introduced by the crystal plasticity, with implicit integration. As demonstrated by Weyler *et. al.* (2012), the penalty method performs quite well in comparison to the more robust and precise method of Lagrange multipliers. In addition, a maximum elastic slip of 0.005 was allowed. Constant friction coefficient of 0.1 is employed in order to mimic phenomena that are not explicitly modelled (for example traction arising from roughness below the resolution of the measurements).

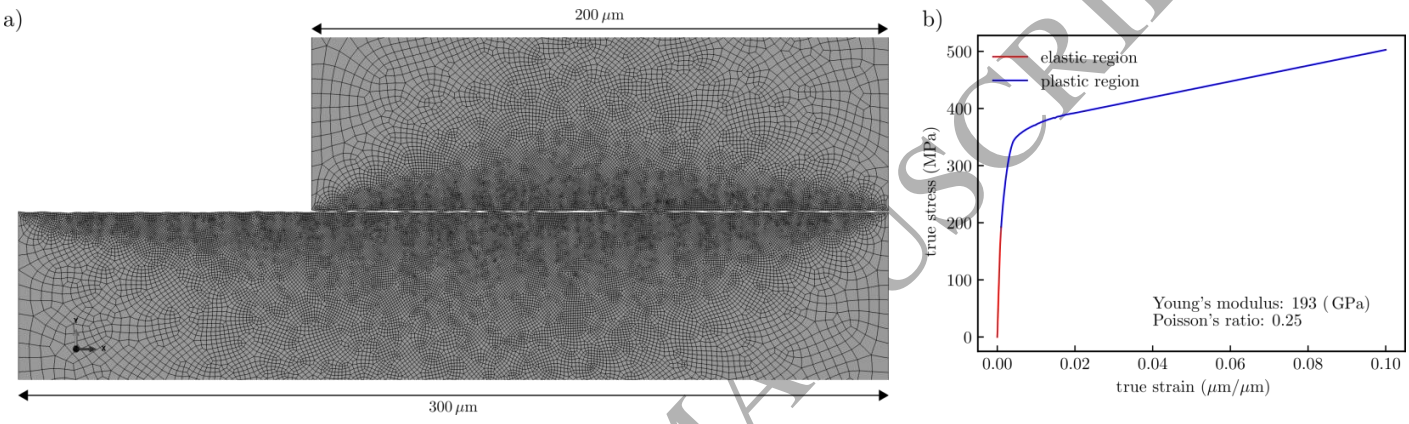

Figure 3. (a) Finite element representation of the upper and lower contacting parts where the rough surfaces are visible at the interface. (b) The isotropic elastic-plastic (Mises) material behaviour initially utilised, representative of a 316 stainless steel.

The material properties implemented are obtained from uniaxial tensile test data for 316 stainless steel (Boyer, 1987) with modulus 193 GPa, and Poisson's ratio 0.25. The model stress-strain behaviour is shown in Figure 3(b).

The normal pressure applied (see Figure 1) is 100 MPa which is representative of the contact stress between a disc and seat in gate valves used in nuclear power plant (Ocken, 1985; Kim *et al.,* 2000). However, austenitic steels will usually have galled at much lower pressures than typical hard-facing alloys. An illustration of the resulting mechanical state (in-plane shear stress) after application of the normal pressure and then at two subsequent stages after normally-loaded sliding is shown in Figure 4.

ACCEPTED MANUSCRIPT

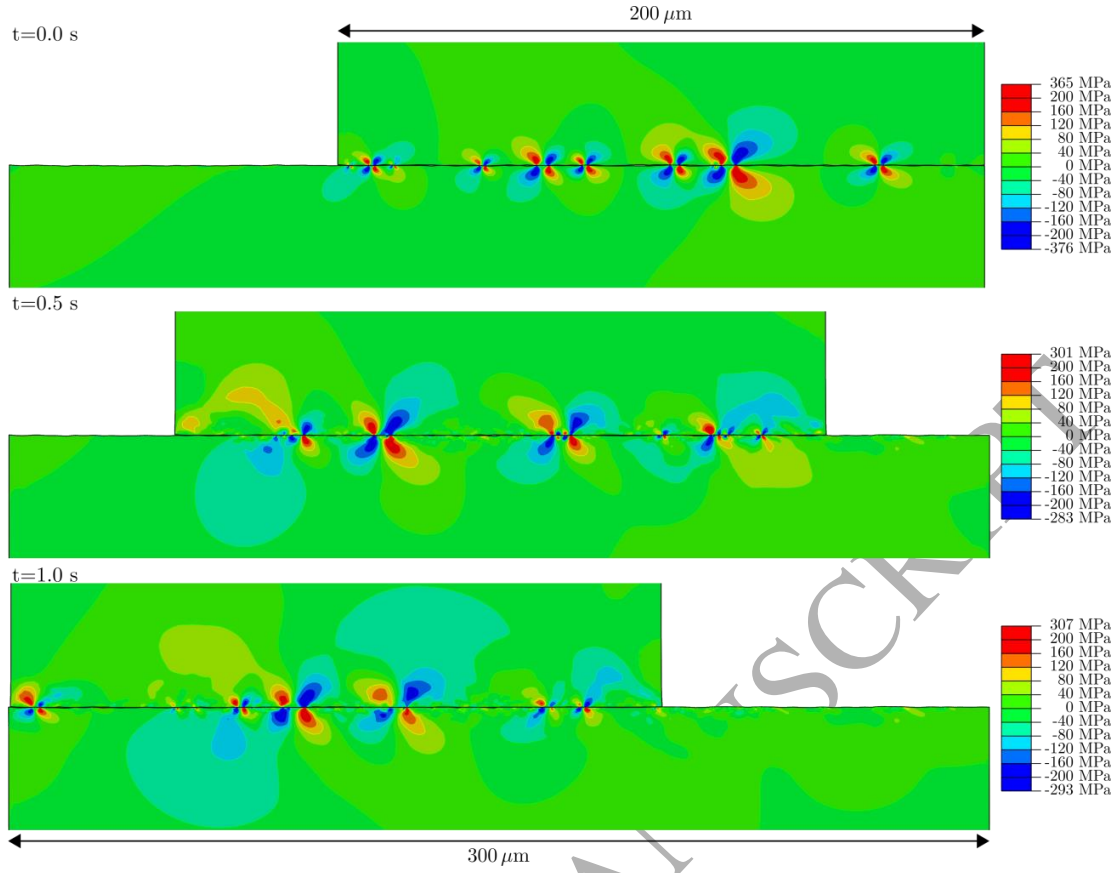

Figure 4. Evolution of stress component σ_{xy} (MPa) after application of the normal loading, and at two subsequent stages during loaded sliding contact. (Sliding is in the x-direction under constant normal loading in the y-direction). A cut-off pressure in the contour plots is set to $\pm$200 (MPa). However, maximum and minimum values are provided at the top and bottom of the legends respectively.

The localized nature of the stress fields established at asperity contact zones is clear and usefully indicative of the length scale which arises by virtue of the surface geometries. Important features are therefore the surface asperity heights, curvatures and separation. However, the key representative dimension driven by the profile geometry and at which investigations are relevant is of order 10 μm. It transpires that despite relatively large normal load, the shear stress is concentrated near asperities in contact and there is no significant bulk deformation or asperity interlocking. A more important quantity to asses is the plastic zone distribution illustrated in Figure 5.

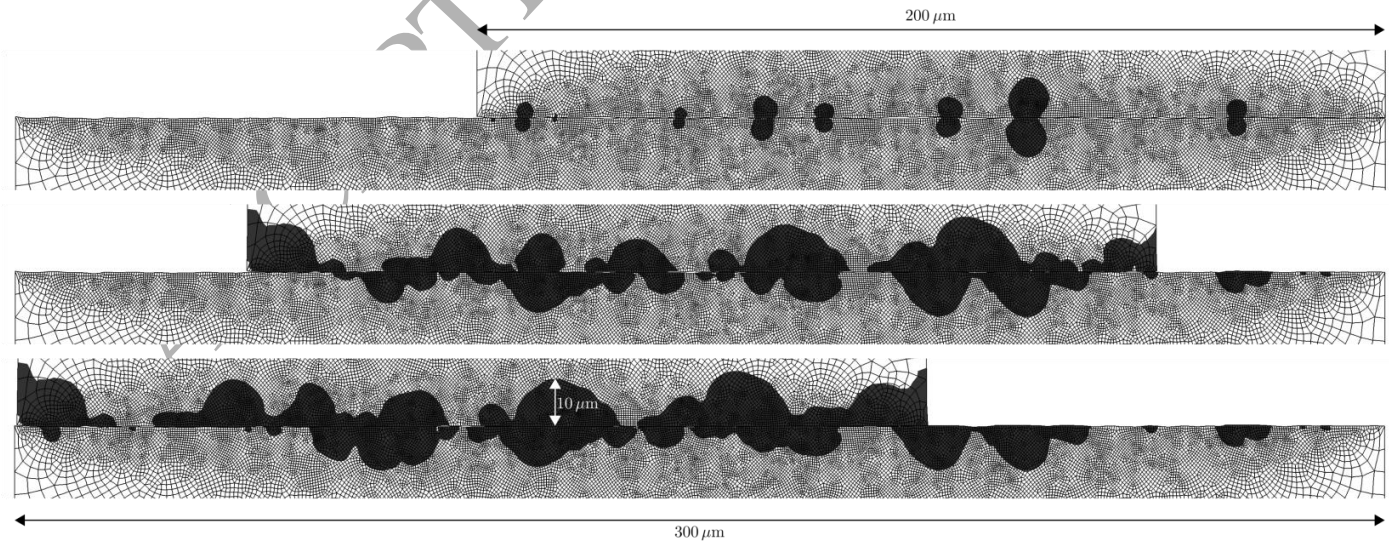

Figure 5. Evolution of the plastic zone (black areas) during sliding using isotropic von Mises plasticity.

The farthest reach of the plastic zone (normal to the interface) is approximately 10 μm. Most hard-facing alloys (of whatever type) have grain sizes between about 2 – 20 μm. The elastic and plastic anisotropy associated with the crystallography is therefore likely to be crucial to the local plastic deformation processes and for this reason, subsequent material behaviour is modelled at the crystal level. In addition, it is argued that in normally-loaded sliding contact for the materials of interest, the key length scale is in fact therefore that of the microstructure, such that grain morphology, crystallography, texture, second phase carbides and silicides, are all likely to be important in the sliding contact behaviour. For this reason, they need to be explicitly included in the investigation and hence the crystal-level modelling methodology is introduced next.

2.3. Crystal slip rule and material properties

In order to explicitly address microstructure in the contact problem, crystal plasticity is introduced for which the crystal slip rule adopted defines the slip rate $\dot{\gamma}^{\alpha}$ on a slip system α (Dunne *et al.*, 2007) by

$$\dot{\gamma}^{\alpha} = \rho b^2 f \exp\left(-\frac{\Delta H}{kT}\right) \sinh\left(\frac{(\tau^{\alpha} - \tau_c^{\alpha})\Delta V}{kT}\right), \tag{2}$$

in which the terms are ρ - density of mobile dislocations, b - Burger's vector magnitude, f - frequency of attempts of dislocations to overcome an energy barrier, H – activation energy, k - Boltzmann constant, T - temperature, τ^{α} and τ_c^{α} - resolved shear stress and critical resolved shear stress respectively, and ΔV - activation volume (assumed constant).

The resolved shear stress is assumed to follow Schmid's law. Hardening is included through evolution of sessile dislocation density following

$$\tau_c^{\text{new}} = \tau_c + Gb\sqrt{\rho_{\text{SSD}}}, \tag{3}$$

which is determined simply from the local plastic deformation

$$\rho_{\text{SSD}}^{\text{new}} = \rho_{\text{SSD}} + \gamma_{\text{st}}\, \dot{p}\, dt \tag{4}$$

where

$$\dot{p} = \sqrt{\frac{2}{3}\boldsymbol{\varepsilon}^{\dot{\boldsymbol{p}}} : \boldsymbol{\varepsilon}^{\dot{\boldsymbol{p}}}} \tag{5}$$

is the effective plastic strain rate and γ_{st} is the hardening coefficient. Material properties were evaluated through calibration by simulating the tests and comparing against experimental results for uni-axial tensile testing on 316L stainless steel (Kang 2010), while anisotropic elastic properties were taken from (Blochwitz, 2005). Both cubic and voronoi tessellated poycrystals were used, the latter generated using Neper software (Quey, 2011). Random grain crystallographic orientation texture was reported for the tested 316L stainless steel which was therefore reproduced in the model polycrystals for the purposes of calibration. The polycrystals and boundary conditions are illustrated in figure 6(a) and (b) respectively, and the resulting calculated averaged polycrystal stress-strain curves are shown in (c) against experimental data. The activation energy and the activation volume were chosen to ensure there was little strain rate sensitivity, as is clear in Figure 6.

ACCEPTED MANUSCRIPT

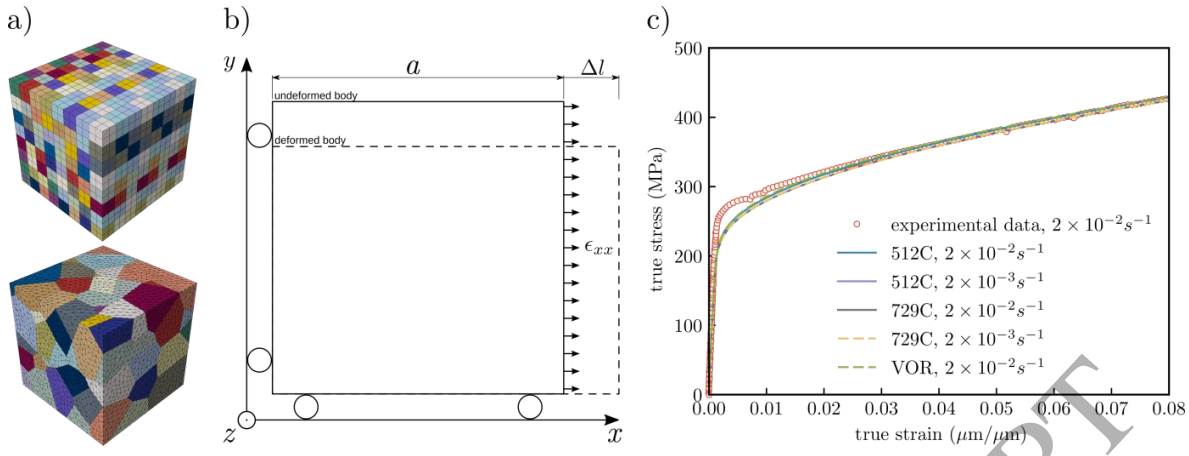

Figure 6. (a) Illustration of two model polycrystals used in calibration (cubic and Voronoi), (b) the boundary and loading conditions (where one of the "in-plane" faces of the cube is also constrained in "z"), and (c) the resulting comparison of averaged polycrystal stress-strain response against experiment. In the middle figure a is a dimension of the cube, while ϵ_{xx} is applied strain. Designation 512C and 729C refer to CPFE models with cubic grains ($8 \times 8 \times 8$ and $9 \times 9 \times 9$ respectively) and VOR to the model with 125 "Voronoi" grains. The models were tested using two different strain rates: $10^{-2}\ s^{-1}$ and $10^{-3}\ s^{-1}$.

The full material properties are detailed in Table 1.

Parameter	Symbol	Value	Unit
Subject to calibration			
Critical resolved shear stress	τ_c	80	MPa
Hardening coefficient	γ_{st}	70	μm^{-2}
Initial density of statistically stored dislocations	ρ_{SSD}	0.0245	μm^{-2}
Constant values			
Burgers vector		2.54	Å
Activation volume	ΔV	4.13×10^{-19}	m^3
Temperature	T	293	K
Frequency of attempts to overcome Peierls barrier	f	10^{11}	s^{-1}
Young's modulus	E	97.8	GPa
Poisson's ratio	ν	0.397	1
Shear modulus	G	125	GPa
Boltzmann constant	k	1.38×10^{-23}	J/K
Activation energy	H	2.60×10^{-20}	J

Table 1. Material properties in CPFE model.

3. Crystal plasticity investigation of sliding contact and galling

The geometric finite element model constructed to incorporate the upper and lower contacting parts, the measured representative hard-facing alloy surface profiles, together with microstructure representation (grain size, crystallography, texture), and friction under sliding contact is similar in scale to that introduced above but now in addition explicitly represents the grains and their crystallographic orientations, and the crystal plasticity. A grain size of 2.55 µm is chosen to be the same as that for the material for which the surface profile measurements were obtained. In the model, we simplify to a uniform grain size and grain shape which is chosen to be hexagonal such that grain boundary discontinuities exist (at the vertices). The morphology was created using VGRAIN software (*e.g.* Cao *et al.*, 2009; Zhang *et al.*, 2011). This simplification means that appropriate refinement of meshing and reasonable CPU times for the analyses become possible. The contact and galling model is shown in Figure 7(a).

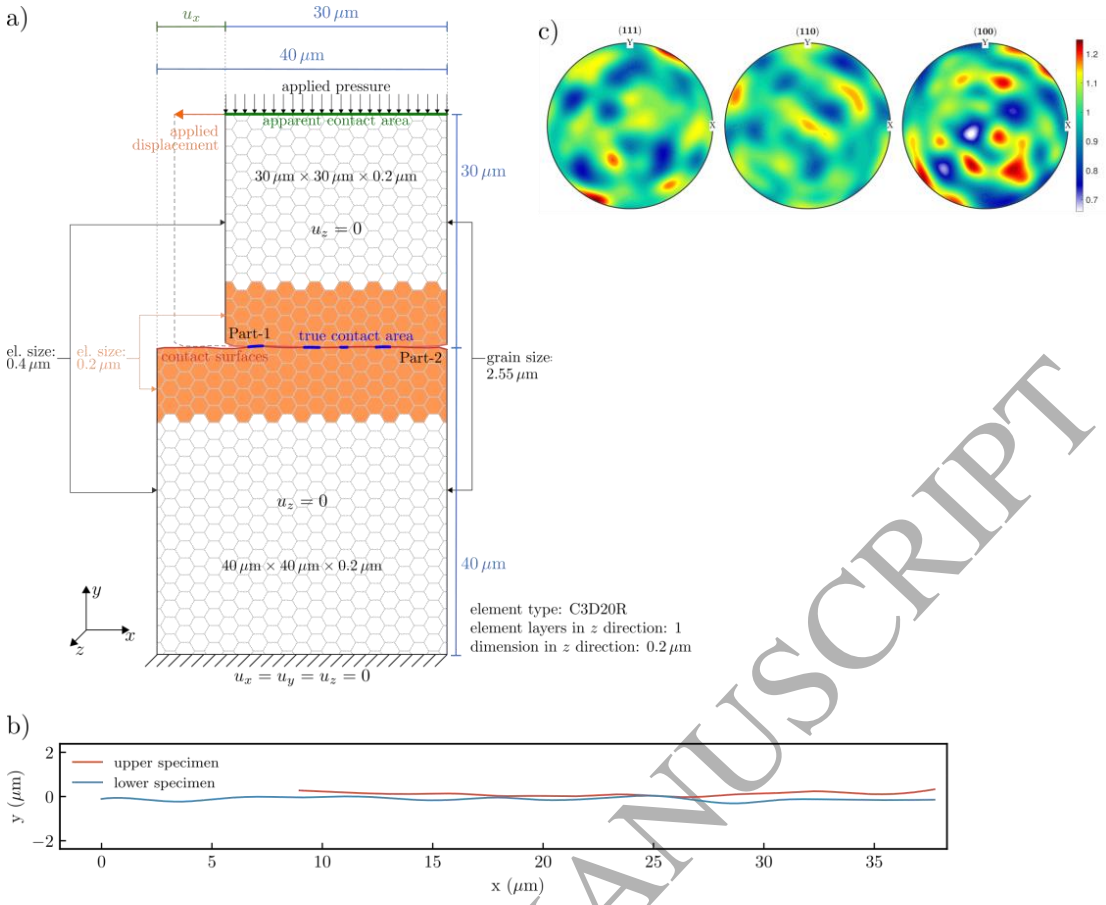

Figure 7. (a) Schematic representation of the contact and galling model showing grain size and distribution, mesh details, loading and the contacting rough surfaces, for which the profiles (upper and lower) are shown in (b), and the orientation distributions (ODF) for the texture in (c). The ODF was visualised using MTEX package (Bachmann *et al.*, 2010).

A mesh refinement study was carried out on the basis of examination of the plastic strain fields established to ensure that no significant change occurred with further refinement. A typical element size for the grains local to the contact region was chosen to be 0.2 μm and a slightly larger size removed from this region as indicated in Figure 7(a). Because of the small grain size considered, a somewhat smaller representative region of the upper and lower parts was modelled, with the corresponding surface profiles shown in Figure 7(b) (which is a sub-region of that considered earlier). Finally, the crystallographic orientations of the grains were assigned to reproduce approximately the random textures (random uniform sampling over rotation group SO(3)), illustrated in Figure 7(c). Note the low intensity values (< ~1.2). As before, the normal (y-direction) pressure applied to the upper part was 100 MPa, followed by displacement of the upper part tangentially (in the negative x-direction) to reproduce sliding contact. The normal and sliding loading steps were named “punch” and “slide” respectively. Each loading step had a duration of 1 s. In both cases automatic incrementation was used with minimum time step 10^{-9} s. The maximum time step was set to 10^{-3} s (“punch”) and $2 \cdot 10^{-4}$ s (“slide”). Such fine refinement was essential to ensure numerical stability, especially during the formation of new contact spots. Figure 8 shows the in-plane shear stress and plastic strain accumulation resulting from the normal loading followed by the sliding contact.

ACCEPTED MANUSCRIPT

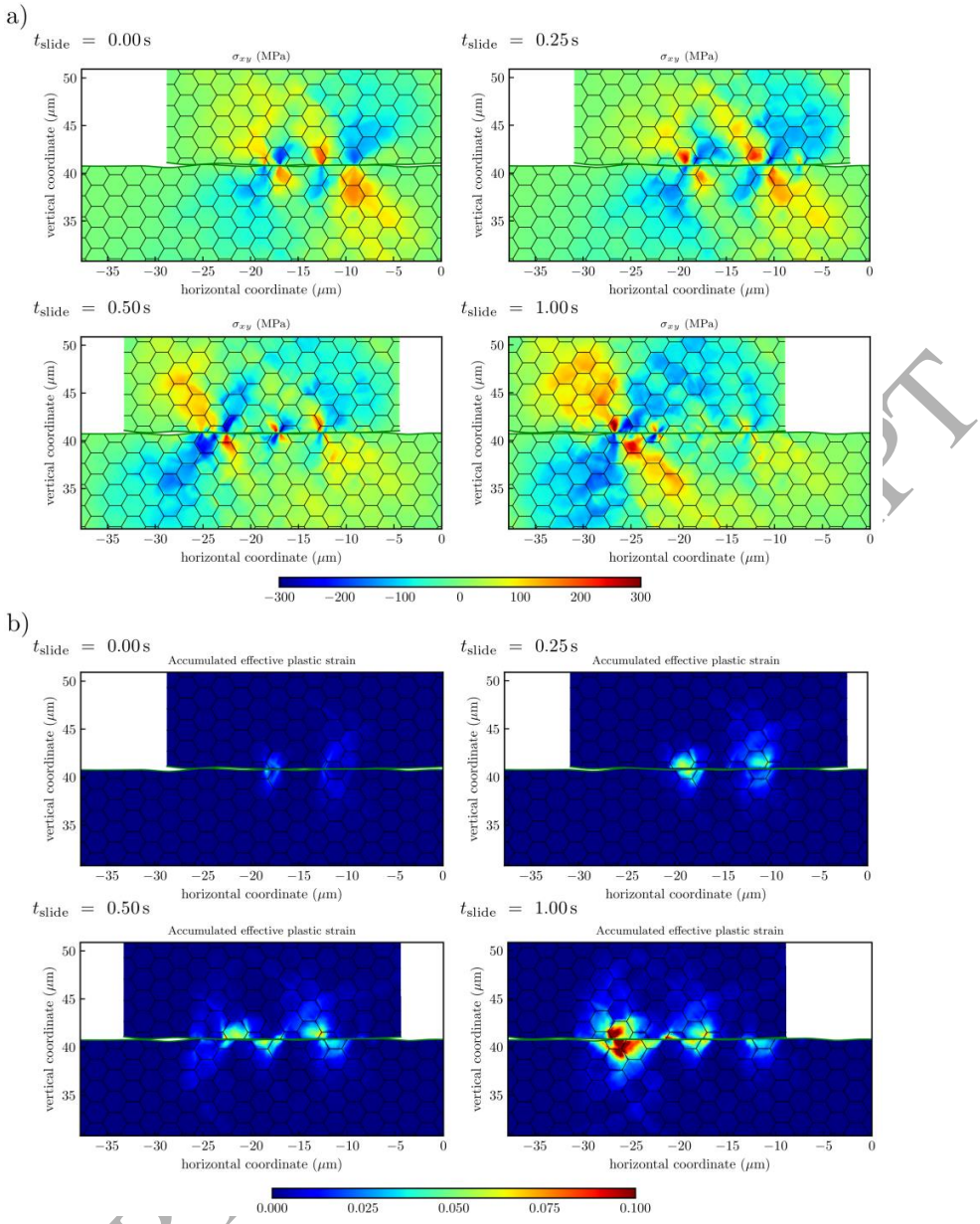

Figure 8. (a) In-plane shear stress component and (b) accumulated plastic strain after normal loading only (t=0), and at subsequent stages of sliding contact (t=0.25, 0.5 and 1.0 s).

The plastic strain remains highly localized at the length scale of the asperity contact (even under relatively high applied pressure at which 316 stainless is known to gall), and largely within a small number of grains. Grain orientation is naturally important since orientations generating low Schmid factors inhibit slip activation, and conversely for those well orientated, thus creating further inhomogeneity locally. It is noted that the normal loading leads to much smaller deformations than those seen by the action of the sliding contact. As anticipated, progressive sliding leads to the evolution of plastic straining both in terms of the magnitude of strains seen and in their spatial reach. The latter quantity is of potential importance since it must reflect the surface depth to which damaging processes may be possible to develop, and which it might be argued are relevant to the galling failure process (qualitatively described above as visual surface damage). The shear stress analysis also demonstrates the establishment of localized and severe sub-surface stresses. This is potentially of significance in the context of local failure in monolithic systems but more so for hard-facing alloys which contain significant fractions of hard carbides of varying sizes ($1-30\,\mu$m) (*e.g.* Ocken, 1995; Cockeram *et al.*, 1997; Kim *et al.*, 2000). It is considered that carbides have positive impact on galling resistance (Boas *et al.* 1977; Budinski, 1981; Cockeram *et al.*, 1997). However, brittle fracture and removal of carbides may affect resistance to wear (*e.g.* Ninham *et al.*, 1988, Atamert *et al.* 1993, Choo *et al.*, 2000; Buchely *et al.*, 2005). Note, however, that carbides (or other hard phases such as silicides) have not been explicitly included in the present study.

3.1. Potential galling indicators

In order to formulate the galling frequency model, it is necessary to find an appropriate way to summarise the mechanical state of the material linked to hazard or survivability functions. In the introduction, many potential properties associated with galling resistance were discussed. Regardless of the proposed indicators the most common denominator is the role of plastic deformation. Hence we focus on the field of accumulated plastic strain and related summary information: magnitude of the plastic deformation, size of the plastic zone and localisation near the contact surface. In order to support this, we also refer to selected theories of wear. One of the earliest examples is by Burwell and Strang (1952), who associate rapid increase of the friction coefficient with critical size of the plastic zone. Some researchers associate probability of wear particle formation with the magnitude of plastic strain and an example is the adhesive wear model introduced by Hornbogen (1975). This approach is related to Suh (1973) delamination theory of wear *i.e.* the release mechanism is based on formation of voids and cracks. The probability is proportional to the ratio of plastic strain and critical strain at which the crack starts to propagate. A similar concept to wear was successfully applied by McCarthy *et al.* (2014) who used earlier research on plastic strain localisation (Manonukul and Dunne, 2004) to develop a criterion for material removal and were able to successfully predict wear track depth in fretting wear. Here we also assess the plastic deformation and its reach. The relevance of localisation is further supported by the view adopted by Vinogradov (1957) and Hsu *et al*. (1980). They argued that in materials more resistant to galling, plastic deformation will be localised near the wear surface. Even if we consider the beneficial role of strain induced phase transformation, researchers (*e.g.* Agarwal *et al.*, 1990; Kim *et al.,* 2000 and Persson *et al.,* 2003) often associate it with modification of mechanical properties.

A number of quantities have therefore been investigated with respect to their relationship with normal load and sliding distance. We investigate evolution of arithmetical mean roughness value R_a (referred to as surface roughness), area of the plastic zone and 99th percentile accumulated plastic strain. The quantities are calculated on the symmetry plane "xy" (the normal vector is perpendicular to loading and sliding direction). Hence, the area of the plastic zone is taken instead of the volume. The 99th percentile of the accumulated effective plastic strain is defined as

$$p_{99}(t,l) = \left\{ p_{\text{eff}}(t,l) : \frac{1}{A_p} \iint_{\mathcal{A}_p} \theta(p_{\text{eff}}(x,y,t,l) - p_{99}) dxdy = 0.99 \right\}, \tag{6}$$

where area of the plastic zone A_p in the cut-off plane $\mathcal{A}$, parallel to loading direction, is formally defined as

$$A_p(t,l) = \iint_{\mathcal{A}} \theta\big(p_{\text{eff}}(x,y,t,l)\big) dxdy \tag{7}$$

The symbol θ corresponds to the Heaviside step function

$$\theta(x) = \begin{cases} 0, & x < 0, \\ 1, & x \geq 0, \end{cases} \tag{8}$$

and $p_{\text{eff}}(x,y,t,l)$ is the accumulated plastic strain at point (x,y) that lies on $\mathcal{A}$, at the given time t and normal load l. This statistic can be viewed as a threshold value that will "cut-out" 99% of the plastic zone. The results are presented in Figure 9.

ACCEPTED MANUSCRIPT

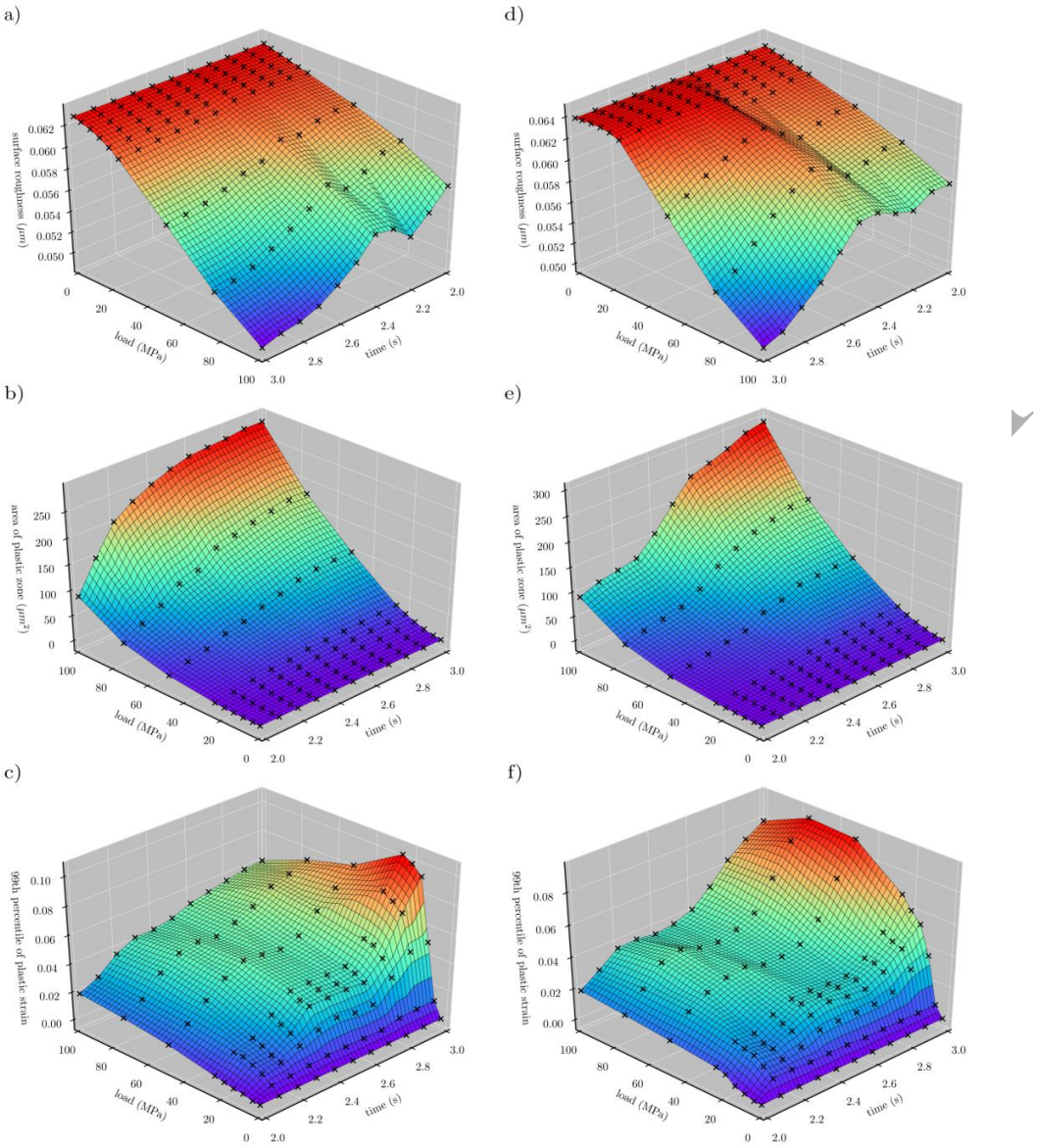

Figure 9. (a), (d) Arithmetical mean roughness value (surface roughness), (b), (e) area of plastic zone, (c), (f) 99th percentile of the accumulated effective plastic strain. Results for the upper galling specimen (upper part of the CPFE model) are presented in (a), (b) and (c), while for the lower galling (lower part of the CPFE model) specimen (d), (e) and (f), as indicated in Figure 1(b). The ”time” scale indicates sliding distance (starting at time 2 s and ending at 3 s).

Each quantity presented represents some aspects of the mechanical state of the system. Deformation of asperities was believed to be a key aspect in galling failure. However, results show that changes of the surface roughness are limited despite application of very high loads. This means that at this scale, defined by the resolution of available surface measurements, asperities can handle loads an order of magnitude above expected galling threshold pressures (for austenitic stainless steels such as 316 or 316L it is approximately 4-8 MPa (ASTM G196)). Hence the hypothesis of asperities flattening and the formation of weld junctions is not supported by the model results. The plastic zone is a non-decreasing function of both sliding distance (step time) and normal load. This is a desired property of a potential galling indicator. However, this measure is potentially too coarse. The 99th percentile is a robust indicator of the saturation of the plastic deformation associated with hardening. From the last frame of the sliding step, it is apparent that this quantity increases with load up to $20-30$ MPa (upper part) and $50-70$ MPa (for lower part). The slight decrease above these stresses can be understood by taking into account information about the size of the plastic zone. Hardening manifests itself by limiting plastic deformation. The areas of very high plastic deformation are located near the contact surface or in the proximity of the first layer of grains. While initially increasing load elevates the deformation at the “hot spots”, due to hardening this effect is limited. Eventually extra work done on the system, with increasing normal load, will result in pushing the plastic zone deeper into the bulk; that is, it is more favourable to initiate slip below the hardened layer, than to increase the plastic deformation near the contact interface. No rapid changes in the volume of plastic zone were observed, in any way indicative of a damaging process.

A more promising candidate for galling indicator is introduced and described as the *plastic reach* as it captures information about the magnitude of plastic deformation as well as its distance from the contact interface. It's argued that greater plastic deformation is associated with higher probability of wear particle formation while greater reach of the plastic zone results in increasing chances of forming fairly large wear particles. This is relevant to the galling mechanisms described by Rabinowicz (1961) as well as those by Vinogradov (1957) and Hsu (1980) who argued that localisation of the deformation near the contact interface is beneficial to galling.

The methodology is as follows. It is demonstrated that the plastic reach follows a power law, as does the cumulative hazard of the Weibull distribution. The latter is appropriate to represent experimental galling data. Hence, if a simple relationship between the plastic reach and the cumulative hazard can be found, then it would allow the establishment of a failure distribution that represents probability of galling (galling frequency), and the latter is derivable solely from the results of CPFE model results without any calibration against galling experiments. Naturally, experimental evidence is required to justify the hypothesis.

In order to define the plastic reach, we introduce the integral measure

$$\mu = \frac{1}{V_c} \iiint_V p_{\text{eff}}(x, y, z) dx dy dz, \tag{9}$$

over an arbitrary sub-volume dV of a body, where the effective accumulated plastic strain is always positive and finite. The next step is to introduce a quantity that represents distance from the contact interface

$$d(x, y, z) = |f(x, z) - y|, \tag{10}$$

where (x, y, z) corresponds to the coordinates of a given point and f is a function that defines the contact surface in the $x - z$ plane. This quantity is based on pseudo-metric

$$d\big((x_1, y_1, z_1), (x_2, y_2, z_2)\big) = |f(x_1, z_1) - y_1| + |f(x_2, z_2) - y_2|. \tag{11}$$

Combining these quantities, one can introduce a family of functionals which represent the magnitude of the plastic strain field with the reach of the plastic deformation:

$$\mu_n = \frac{1}{V_c} \iiint_V d^n(x, y, z) p_{\text{eff}}(x, y, z) dx dy dx, \tag{12}$$

where normalisation coefficient V_c is called the characteristic volume. The value of μ_n is referred to as the n-th moment of plastic reach, while for the case $n = 1$ it is simply plastic reach p_R. Hence, if V_c is equal to volume of the plastic zone, then $\mu_0 = \overline{p}_{\text{eff}}$ *i.e.* mean accumulated effective plastic strain. The concept of plastic reach is illustrated in Figure 10. For each normal applied load, a punch-slide CPFE simulation was preformed and the moments of the plastic reach extracted from the last frame of the simulation. Furthermore, it was assumed that $V_c = 1$. (This is explained in the following section.) Results of the analysis are presented in Figure 11.

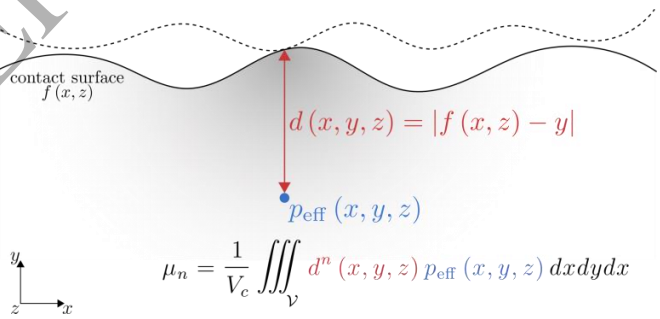

Figure 10. The concept of the moments of plastic reach.

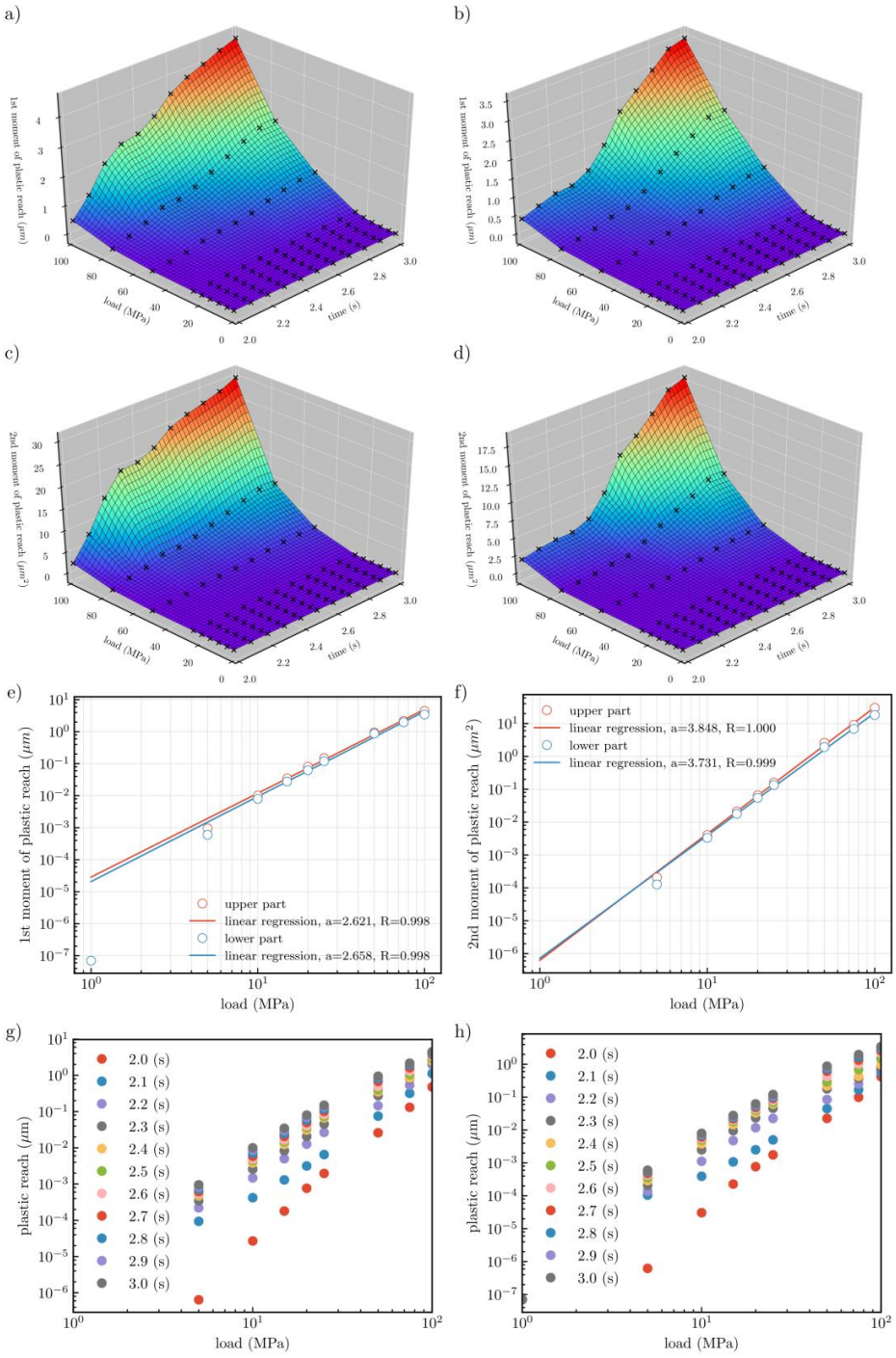

Figure 11. First and second moment of plastic reach (sub-figures a - d) as a function of normal load and sliding step time (2.0 s - 3.0 s). The sliding step time was preceded by contact initiation (0.0 s - 1.0) and application of normal load (1.0 s - 2.0 s). Sub-figures (a) and (c) correspond to the upper galling specimen of the model (upper part of the CPFE model) while (b) and (d) represent the lower galling specimen (lower part of the CPFE model). 1st and 2nd moments of plastic reach plotted on log-log axes are presented in sub-figures (e) and (f). These values correspond to the last frame of the sliding (t =3.0 s in the simulation time). Finally, (g) and (h) are showing the limiting values of plastic reach in terms of the sliding distance for upper and lower part respectively.

It transpires that the moments of plastic reach are non-decreasing functions of the normal load, which is a desired property since it can be directly linked with cumulative hazard. In addition, the plastic reach follows a power law relation for loads higher than ≈ 10 MPa. This has been quantified by evaluation of the Pearson correlation coefficient R. In all cases values of R are approximately 1. Figs. 11 (g) and (h) indicate that final sliding distance was appropriate and sufficient to draw quantitative conclusions since a near-saturated state has been achieved.

3.2. Linking plastic reach with galling probability

On the basis of the approach presented by Zok (2017) we can express cumulative hazard in terms of its estimates evaluated on a representative section (see appendix B). Selecting the Weibull distribution to link with the plastic reach essentially defines the form of cumulative hazard H

$$H = \frac{V}{nV_m}\langle H_0\rangle = \left(\frac{l}{l_0}\right)^{\beta}, \tag{13}$$

where l_0 is the scale and β the shape parameter. Both of these parameters are determined from the plastic reach evolution from the sliding contact CPFE calculations as outlined below. The ratio V/nV_m, is that between the total volume of interest in a specimen (where deformation is expected to be non-negligible) and the chosen representative volume. The latter simply translates to n subdivisions with constant volume V_m. In other words, we infer on the basis of representative sub-volume nV_0, in n steps, and by considering models of volume V_m one at the time. (See Appendix C.) A Weibull distribution was selected on the basis of desired properties: $F(l) \to 1$ as $\to \infty$, $F(l) \to 0$ as $l \to 0$ (Zok, 2017; Weibull 1939), and was justified on the basis of experimental data analysis (see Appendix D). The plastic reach has the same properties and can be well approximated by a power law, as shown in Figure 11. Summarising the reasoning described in Appendix C, it is postulated that there is a functional relationship $\mathcal{G}$ between cumulative hazard rate H and the plastic reach $p_R^{(V)}$,

$$H(l) = \mathcal{G}\left(p_R^{(V)}(l)\right), \tag{14}$$

where $p_R^{(V)}(l)$ is defined as

$$p_R^{(V)} = \frac{1}{V}\iiint_V d(x,y,z)p_{\text{eff}}(x,y,z,l)dxdydx. \tag{15}$$

Here, integration is carried out over the whole volume of interest. Furthermore, it is postulated that this relation is

$$H(l) = \left(\frac{l}{l_0}\right)^{\beta} \propto \langle p_R(l)\rangle \text{ if } l > l_0. \tag{16}$$

where $p_R(l)$ is averaged over values of plastic reach (with unit characteristic volume) evaluated for subdivisions of volume V_m. It is assumed that for $l < l_0$ there is a saturation effect associated with hazard rate, which is negligible above certain values. Expressing the proportionality with a single meta-parameter γ gives

$$H(l) = \gamma\langle p_R(l)\rangle. \tag{17}$$

For now, it is assumed that the single CPFE model is sufficient to provide good approximation of the estimate $\langle p_R(l)\rangle$. Finally, the galling frequency/probability F is

$$F(l) = 1 - \exp\big(-H(l)\big) = 1 - \exp\big(-\gamma p_R(l)\big) = 1 - \exp\left(-\left(\frac{l}{l_0}\right)^{\beta}\right). \tag{18}$$

Note that first term in the chain of equations is true for any distribution. Since the reasoning is based on the fact that p_R can be approximated by a power law, one can evaluate values of the shape parameter β from the relation

$$\ln p_R(l) = \beta(\ln l) + (-\ln\gamma - \beta \ln\ l_0). \tag{19}$$

using the results obtained from CPFE simulations above - $(\ln p_R(l), \ln l)$ *i.e.* from the log-log relation between plastic reach and normal load (Figure 11 (e)). An important quantity to evaluate is the scale parameter l_0 which, from the expression for the galling frequency above, indicates that it defines the normal load regime over which galling occurs. The basis for the hypothesised measure of galling introduced, namely plastic reach, suggests the importance of a further quantity. That is, when the two rough surfaces are brought in to contact, and the normal loading applied, firstly the contacting asperities deform elastically, which is followed by the onset of local yield – *i.e.* at the crystal contact level, the initiation of slip. The normal applied load necessary to cause first slip, quantified in the CPFE calculations as that load giving rise to the first local achievement of an effective plastic strain of 0.2%, is argued to be a sensible measure to identify a representative loading

ACCEPTED MANUSCRIPT

regime (for a given surface with roughness and microstructure). Detailed analysis of multiple punch-slide simulations reveals that the first microscopic (0.2%) yield point also corresponds to the minimum load l_0 above which $\ln p_R(l)$ starts to vary linearly with $\ln l$. This approach is consistent with theories of wear, including Archard (1956), Rabinowicz, (1973) and Hornbogen (1975). Formally l_0 is defined as

$$l_0 = l: \max\left(p_{\text{eff}}(x, y, z, l)\right) = 0.002. \tag{20}$$

Hence on this basis, the CPFE surface contact crystal plasticity models provide the methodology by which the two key Weibull properties, l_0 and β may be determined (using Figure 11 (e) and (f)) such that predicted galling frequency distribution may be obtained. The overall methodology is summarised in Figure 12, giving predicted Weibull parameters of $l_0 = 9.48$ and β =2.64 together with the predicted galling frequency distribution for 316L steel at 20°C, also shown in Figure 12, compared to independent experimental data. The CPFE predicted value of the β parameter is an average over results for the lower and upper model parts and is found to be close to independent values for the Weibull distribution obtained by fitting to experimental data (reported in Appendix D).

ACCEPTED MANUSCRIPT

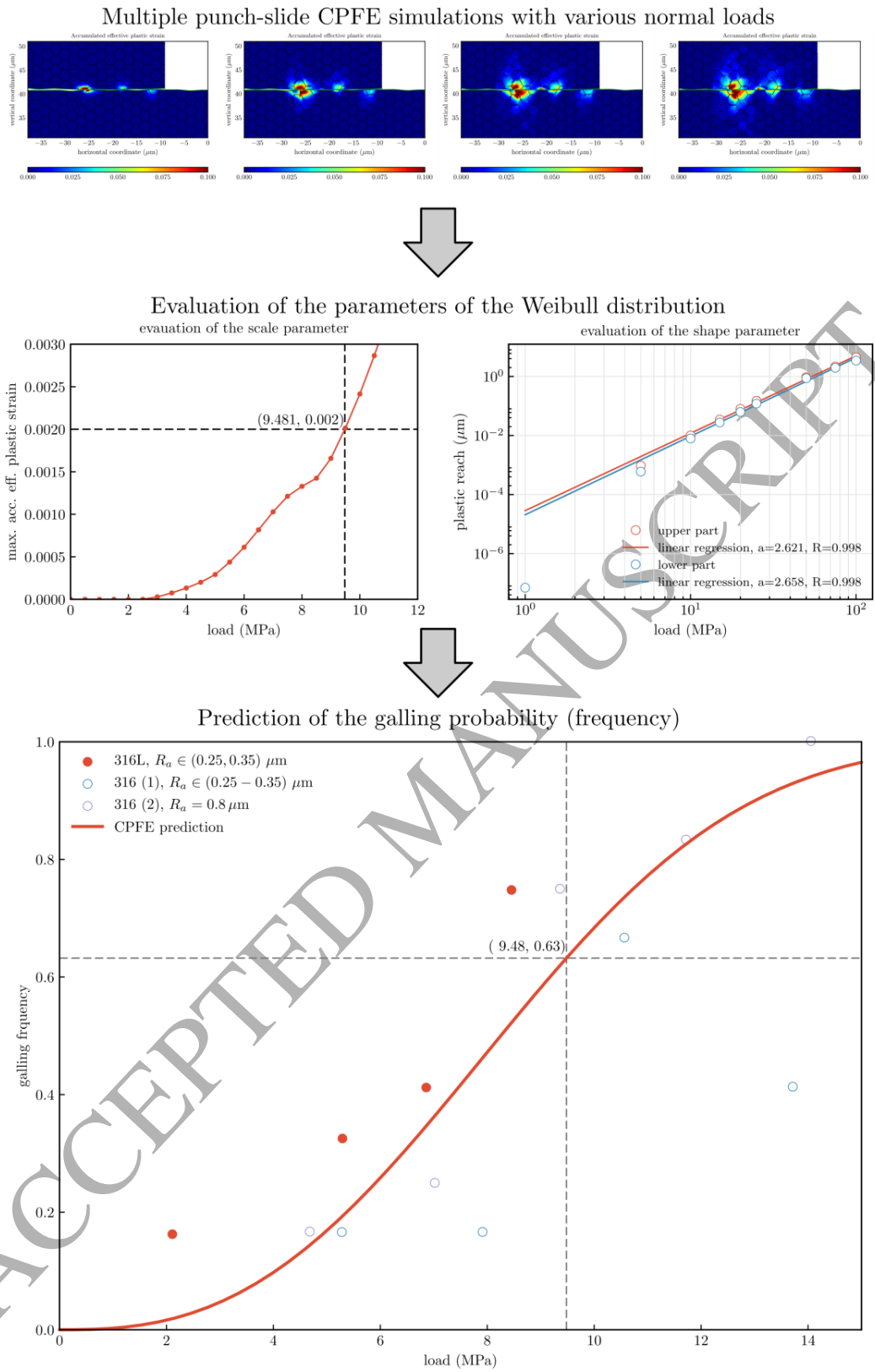

Figure 12. Predicted Weibull galling frequency determined from a series of punch-slide CPFE simulations carried out at different normal load. Predictions are compared with experimental data taken from Hummel *et al.* (2009) and Harsha *et al.* (2016).

It transpires that predicted galling frequency is in reasonably good agreement with experimental data. However, the experimental data are provided without any confidence bounds. Some insight in to how large the uncertainties are is provided by the data set marked as 316 (1). In this case, the highest galling frequency was reported for the second largest normal load.

ACCEPTED MANUSCRIPT

It's anticipated that such an observation would be rather unlikely if sufficient numbers of samples was tested. An assessment of how well the Weibull (and other) distributions represents galling frequency in 316 steel is presented in Appendix D, and in addition shows that the fitting of the Weibull distribution directly to data for 316 steel gives average shape factor of 2.42, compared with the CPFE predicted value obtained from the plastic reach above of 2.62 and 2.65 for the lower and upper parts respectively. Assessing confidence intervals for the predicted galling frequencies is necessary and presented in the next section. However, a more qualitative indication of predicted galling trend with surface roughness variation is considered against independent data in the literature (Podgornik et al, 2004) and shown in Figure 13.

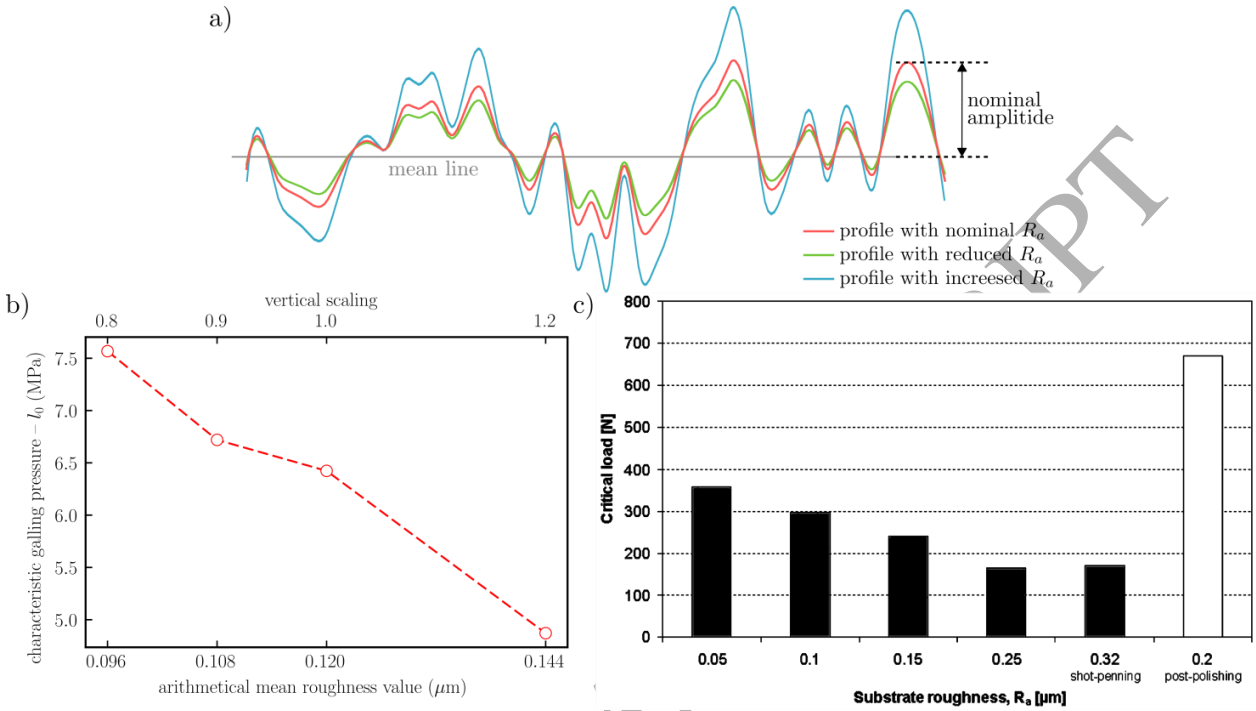

Figure 13. showing (a) surface roughness variations considered, and the qualitative comparisons (for two different material systems) of (b) model predicted galling load for 316 steel and (c) independent experimental data for a stainless steel (Podgornik et al, 2004)

The latter galling assessment is based on single-stroke sliding test on a stainless steel and the propensity for steel transfer to the TiN coated tool steel. A decreasing contact load is observed with increasing surface roughness as is predicted for this surface profile by the galling model, although the magnitudes of the galling loads are very different for the two materials considered. In addition, as often for galling experiments, no further details (other than roughness) on the surface profiles are provided, but it is noted that other surface features (*e.g.* wavelength, asperity curvature) are also predicted by the model to be important in galling, as later study by Podgornik *et al.* (2012) showed.

The mechanistic basis for galling proposed is that plastic strains of sufficient magnitude and reach (*i.e.* depth in to the deforming surface) are required to generate local rupture at contacts and hence the creation of new abrasive particles of sufficient size between the contacting surfaces in order to drive galling failure. The plastic reach metric is, in effect, an indirect measure of damage. Explicit modelling of material separation and the generation of particles at the interface would require a material separation (*i.e.* damage) law. In addition, in more complex materials containing hard (*e.g.* carbide or silicide) particles, it is known that particle pull-out occurs and this also would need an explicit incorporation of material separation if it were to be modelled in full. However, it may be the case even in the latter circumstances that the plastic reach captures the onset of the conditions necessary to drive particle decohesion, and hence generation of abrasive wear debris. However, clearly further studies of the failure processes are needed to assess how best to represent them in predictive models.

3.3. Confidence intervals on predictions of galling probability

The final consideration is the repeatability of determined galling frequencies. In this section, knowledge obtained from multiple CPFE analyses is combined to provide better estimates and also to quantify the model confidence level. Model results are extracted for many differing contact interfaces (roughness profiles) and texture realisations. From the same generic experimental profile, multiple surface samples were selected. The sampling strategy is illustrated in Figure 14.

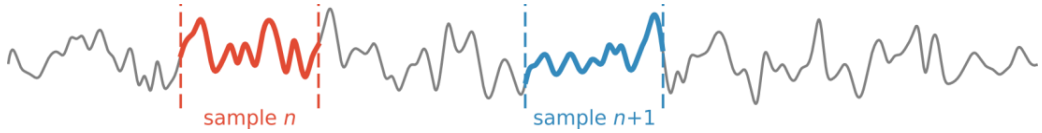

Figure 14. The concept of selection of a new profile for the contact interface.

Each pair of profiles was used to generate a new CPFE model using the method described in the previous section. In each case, the texture was generated using random uniform sampling over rotation group SO(3). Following the procedure introduced earlier, for each model, plastic reach p_R as a function of normal load was evaluated. This study involved at least five punch-slide simulations with different values of the normal load, performed on three different CPFE models with distinctive profiles and textures. Full detail is presented in Appendix E. The results are illustrated in Figure 15.

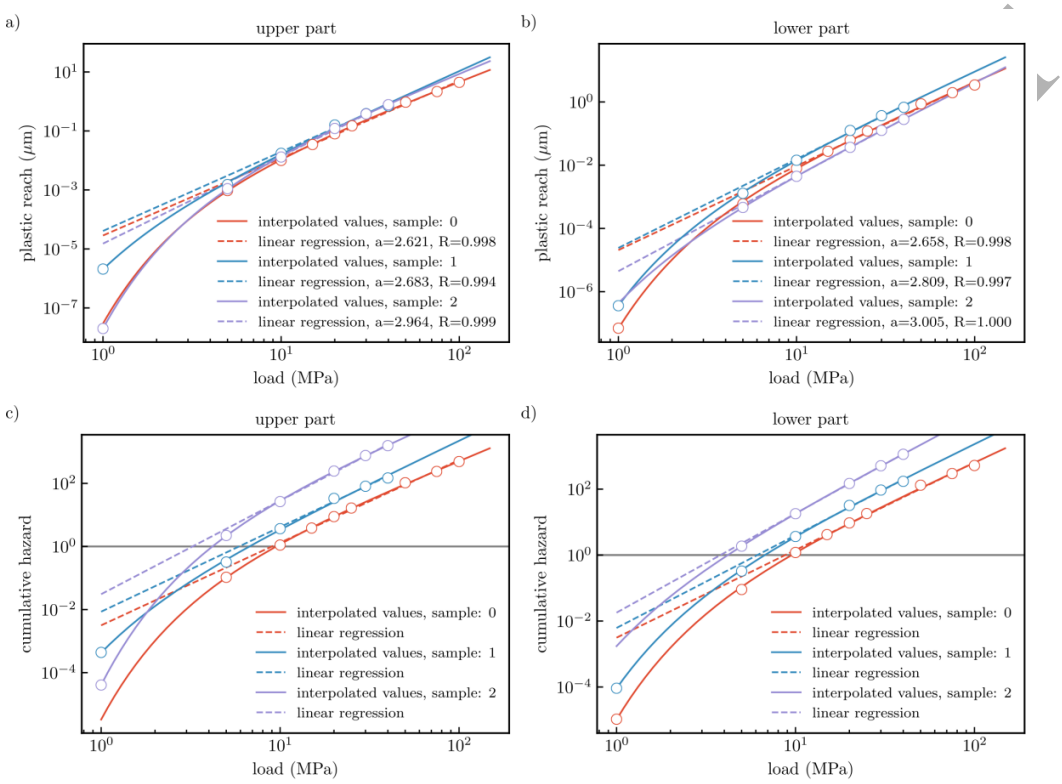

Figure 15. Evaluation of plastic reach and cumulative hazard from a series of differing profiles and textures and punch-slide simulations; (a) and (b) plastic reach as a function of normal load evaluated for upper and lower parts respectively; (c) and (d) corresponding cumulative hazard function.

Estimated confidence bounds are illustrated in Figure 16. Note that they are associated with a single estimate, as opposed to the expected value.

ACCEPTED

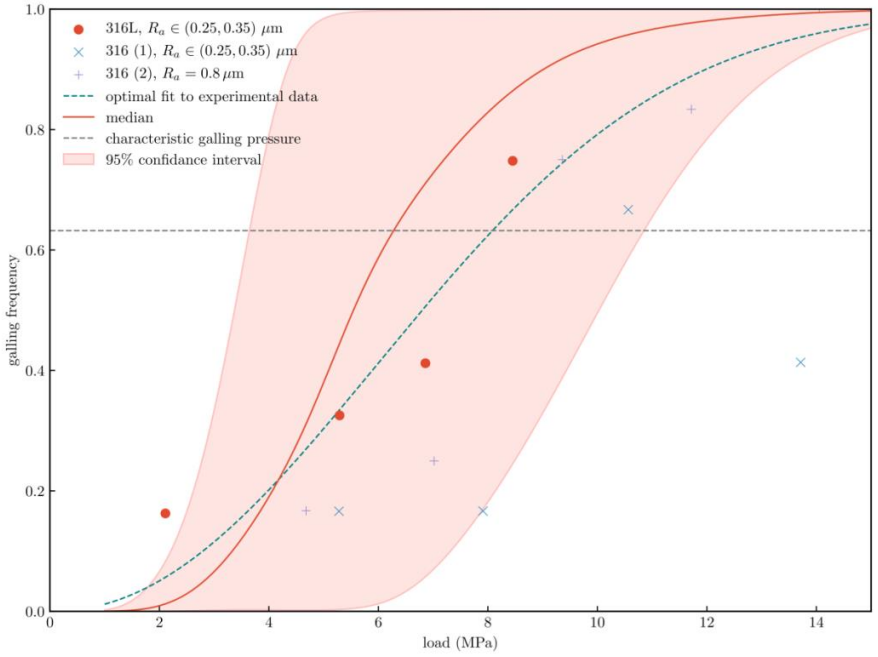

Figure 16. Confidence interval compared with experimental data, an optimal least-square fit of a Weibull distribution to the experimental data for 316L steel. Data were taken from Hummel (2009) and Harsha (2016).

We note that the repeatability study gives rise to broad bounds on the predicted galling loads. One key factor not addressed in the current methodology is that of the full three-dimensional nature of real surfaces in contact. The model geometries utilised for the contacting surfaces are quasi-3D in that the 2D surface profile, *e.g.* in Figure 2, is assumed to be prismatic out of plane in the 3D contact models shown in Figure 7 and subsequently. The simplification is to make the calculations tractable but a consequence is (i) far fewer contacts than would actually interact, and (ii) simplified in-plane stress and plastic strain states developed at the contacting asperities, even though out-of-plane stresses and strains are allowed but for the prismatic profile. For both of these reasons, the galling frequency predictions will not completely describe true 3D surfaces in contact and likely for the former of the two, and as demonstrated by the arbitrary repeatability testing, the broad range in predicted galling load bounds occurs. The median galling prediction in Figure 16 differs from the optimal fit to the experimental data, and it is feasible that this results predominantly from the latter of the two factors.

4. Conclusions

A new methodology has been introduced which explicitly represents the geometry of contacting surfaces and the underlying material microstructural features at an appropriate length scale in order to investigate sliding contact of rough surfaces under normal loading. A new metric, the plastic reach, for contacting surfaces has been introduced which provides a quantitative measure of the magnitude and spatial reach of the local plasticity developing at contacting surface asperities under normally loaded sliding contact. This is argued to be a metric with which to quantify the onset of galling failure. The mechanistic basis proposed is that plastic strains of sufficient magnitude and reach (*i.e.* depth in to the deforming surface) are required to generate local rupture at contacts and hence the creation of new abrasive particles of sufficient size between the contacting surfaces in order to drive galling failure.

The plastic reach has been shown to be related to a hazard function and because of its power law relationship to applied normal loading, it has been possible to establish the relationship between the Weibull frequency for galling failure and the plastic reach. Hence for metal to metal rough contacting surfaces, a quantitative definition of galling has been introduced. The galling load, which specifies the 0.63 Weibull probability of galling failure, is given by the applied normal load necessary to drive the first local slip at contacting asperities to an effective plastic strain of 0.2%. The shape factor associated with the Weibull frequency distribution is given by the predicted power law relationship between plastic reach and applied normal loading. Hence, galling load has been predicted from knowledge of material and contacting surface properties without any additional parameterisation. Predicted galling frequency for a 316L stainless steel has been determined from knowledge of the surface profile geometry, the texture, grain size and the fundamental crystal properties (slip strength and hardening). Qualitative comparisons with independent experimental measurements of galling frequency have been obtained and the confidence levels in the predictions have been quantified.

The methodology established includes the roles of material (crystal) properties, microstructure (morphology and crystallographic orientation), and surface properties (roughness, wavelength and asperity geometry) in addressing galling, but

further work is necessary to consider the potentially important aspects of oxide layer formation and break-away, and phase transformation at contacting surfaces.

5. Acknowledgments

B. Barzdajn would like to thank Rolls-Royce plc and Imperial College London for supporting this research. F. P. E. Dunne wishes to acknowledge gratefully the provision of funding for his Royal Academy of Engineering/Rolls-Royce research chair.

Appendix A. Stochastic approach to galling

The standard approach assumes that for given value of normal load l there is a specific probability of galling $P(l)$, in this case defined as the fraction of samples that gall

$$\frac{\text{number of samples that galled}}{\text{number of tested samples}} = P(l). \tag{21}$$

It is reasonable to assume that the galling probability/frequency should have the properties of a cumulative distribution function (CDF). For a valid galling experiment (in practice or in a model representation), all samples are made from the same batch of a material and machined in the same way. As a result, properties such as the distribution of microstructural features, phase fractions or parameters describing the contact surfaces are also the same or at least very similar. Different outcomes under the same conditions must result from variations (such as in texture, morphology, surface profile) between samples. For each tested sample, there is an associated property called intrinsic galling threshold pressure, L. This property should in principle be related to physical properties yet to be determined. Each experiment results in galling when the applied normal load $l > L$. Hence, each single test is statistically modelled, by replacing the unique value of L with an underlying distribution. The distribution represents the variation of intrinsic galling threshold pressure across all tested samples. A cumulative distribution function F associated with probability of galling failure may then be introduced and modelled by a random variable, which we label in the same way (*i.e.* as L). The function F is related to the galling probabilities by $P(l > L) = F(l)$ and $P(l < L) = 1 - F(l)$. Consider a scenario in which a tested sample hasn't galled under a normal load l. The probability that an identical sample galls after increasing the load by Δl is given by the conditional probability

$$P_l(\Delta l) = P(l < L \leq l + \Delta l | L > l), \tag{22}$$

The vertical bar symbol is used to express the notion of "given". Next, the hazard rate is introduced which is the probability P_l in the limit of infinitesimal increase of galling pressure i.e. $\Delta l \to 0$. Bayes theorem gives

$$P(l < L \leq l + \Delta l | L > l) = \frac{P(l < L \leq l + \Delta l) P(L > l | l < L \leq l + \Delta l)}{P(L > l)}. \tag{23}$$

If F represents the associated cumulative distribution function, and given that $P(L > l | l < L \leq l + \Delta l) = 1$ (if $l < L \leq l + \Delta l$ the condition $L > l$ is already satisfied), then

$$P(l < L \leq l + \Delta l | L > l) = \frac{P(l < L \leq l + \Delta l)}{P(L > l)} = \frac{F(l + \Delta l) - F(l)}{1 - F(l)}. \tag{24}$$

Formally the hazard rate $h(l)$ is defined as

$$h(l) = \lim_{\Delta l \to 0} \frac{P(l < L \leq l + \Delta l | L > l)}{\Delta l}. \tag{25}$$

Hence, using the previous relation

$$h(l) = \lim_{\Delta l \to 0} \frac{1}{\Delta l} \frac{F(l + \Delta l) - F(l)}{1 - F(l)} = \frac{f(l)}{1 - F(l)}, \tag{26}$$

where $f = dF/dl$ can be interpreted as a distribution of "intrinsic galling pressure" across all possible samples. The hazard rate can be interpreted as a continuous limit of the ratio between the number of samples which galled after increasing the load by Δl and samples that haven't galled up to the load l. In failure analysis, the quantity

$$S(l) = 1 - F(l) \tag{27}$$

is probability of survival, also called survivability. We can relate hazard rate, also known as force of mortality, with survivability in the following way

$$h(l) = \frac{f(l)}{S(l)} = \frac{\frac{\mathrm{d}}{\mathrm{d}l} F(l)}{S(l)} = \frac{-\frac{\mathrm{d}}{\mathrm{d}l}\big(1 - F(l)\big)}{S(l)} = \frac{-\frac{\mathrm{d}}{\mathrm{d}l} S(l)}{S(l)}. \tag{28}$$

Using the chain rule this relation can be rewritten as

$$h(l) = -\frac{\mathrm{d}}{\mathrm{d}l} \ln\big(S(l)\big). \tag{29}$$

Integrating over l yields a quantity called the cumulative hazard function H

$$H(l) = \int_0^l h\,(x)\mathrm{d}x = -\ln\big(S(l)\big). \tag{30}$$

Cumulative hazard can be linked with survivability in a similar fashion

$$S(l) = e^{-\int_0^l h(x)\mathrm{d}x} = e^{-H(l)}. \tag{31}$$

Using equation (27) the probability of failure becomes

$$F(l) = 1 - e^{-H(l)}. \tag{32}$$

Appendix B. Weakest link approach and representative volume I

The aim is to identify a mechanical state that is responsible for initiation of macroscopic galling. In order to describe the failure of a macroscopic volume, it may be sufficient to use representative fragment/fragments of the macroscopic tribosystem, assuming that the triggering effect is associated with sufficiently small scale. We divide the region of contact into N equal sections and assign probability of survival S_{0i} to each one of them. It is assumed that this division does not go below the relevant scale. Furthermore, let each one of them be associated with a development of a microstate Γ_i. From the weakest link approach one can say that galling will not occur, when none of them will "fail". We introduce similar reasoning as was presented by (Zok, 2017). Probability of survival S of the whole system, from basic properties of probability is

$$S(l) = \prod_{i=1}^{N} S_i\left(\Gamma_i(l)\right), \tag{33}$$

where N is the number of divisions, S_i is the survivability of the i-th section while $\Gamma_i(l)$ is a mechanical state developed at i-th location as a result of load l. The survivability may vary across the body due to *e.g.* pre-existing local defects. However, assume that S_i depends only on the state $\Gamma_i(l)$ *i.e.* $S_i\big(\Gamma_i(l)\big) = S_0\big(\Gamma_i(l)\big)$. As a result

$$S(l) = \prod_{i=1}^{N} S_0\left(\Gamma_i(l)\right). \tag{34}$$

ACCEPTED MANUSCRIPT

Applying logarithms yields

$$\ln S = \sum_{i=1}^{N} \ln S_0\big(\Gamma_i(l)\big). \tag{35}$$

Combining the above relation, with the property of accumulated hazard $H(l) = -\ln\big(S(l)\big)$, derived in previous section, one can write

$$\ln S = \sum_{i=1}^{N} \ln S_0\big(\Gamma_i(l)\big) = N\frac{1}{N}\sum_{i=1}^{N} \ln S_0\big(\Gamma_i(l)\big) = -N\frac{1}{N}\sum_{i=1}^{N} H_{0i}\,(l) = -N\langle H_0\rangle, \tag{36}$$

where H_{0i} is a cumulative hazard of section i and $\langle H_0\rangle$ is the average over them. Given that the number of divisions N is defined by the ratio of the system and section volume, i.e. $N = V/V_0$

$$\ln S = \sum_{i=1}^{N} \ln S_0\big(\Gamma_i(l)\big) = -\frac{V}{V_0}\langle H_0\rangle, \tag{37}$$

where $H_0 = \ln S_0\big(\Gamma_i(l)\big)$ is a cumulative hazard associated with i-th section and $\langle H_0\rangle$ is an estimator of expected value $E(\{H_{0i}\})$ represented by average cumulative hazard. In case of homogeneity the average will converge fairly fast allowing predicting survivability from representative sections of the bulk.

Appendix C. Weakest link approach and representative volume II

The weakest link approach allows expressing hazard of a macroscopic body in terms of estimates evaluated on representative fragments (see appendix B)

$$H_V \approx \frac{V}{V_0}\left\langle\left\{H_0^{(i)}(l)\right\}\right\rangle_V. \tag{38}$$

Here l is normal load, V is volume of interest within the specimen (where deformation is expected to be non-negligible), H_V associated cumulative hazard, and $\left\{H_0^{(i)}\right\}$ is set of cumulative hazards related to section $V_0^{(i)}$ with volume V_0. Index in the average indicates region of averaging. For the sake of simplicity, it is assumed that partitioning of V is such that $V/V_0 = N$ and $N \in \mathbb{N}$. Functional relationship is postulated, between average (representative) cumulative hazard and plastic reach

$$\left\langle\left\{H_0^{(i)}(l)\right\}\right\rangle_V = \mathcal{G}\left(p_R^{(V)}(l)\right), \tag{39}$$

where plastic reach summarizes state of the whole specimen and it is defined as

$$p_R^{(V)}(l) = \frac{1}{V}\iiint_V d(x,y,z)p_{eff}(x,y,z,l)dxdydz. \tag{40}$$

Simple relation of proportionality is assumed, *i.e.*

$$\left\langle\left\{H_0^{(i)}(l)\right\}\right\rangle_V \approx \alpha p_R^{(V)}(l). \tag{41}$$

Both sides of the above are referring to quantities that are independent of the specimen dimensions. Hence they will be dependent only on the material and local surface properties. Combining (38), (40) and (41) allows expressing cumulative hazard in terms of the integral that is equal to plastic reach with unit characteristic volume

$$H_V \approx \frac{\alpha}{V_0}\iiint_V d(x,y,z)p_{\text{eff}}(x,y,z,l)dxdydz. \tag{42}$$

ACCEPTED MANUSCRIPT

The integral has unit μm^4. Hence, α must be proportional to μm^{-1}. In consequence α defines the length scale. Subsequently, an extended partitioning strategy is introduced to replace $p_R^{(V)}(l)$ with its estimate. This strategy is illustrated in figure C1.

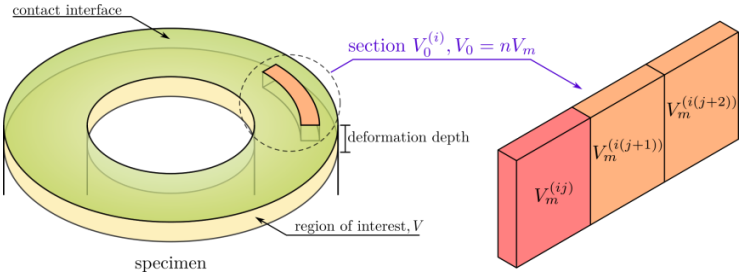

Figure C1. The partitioning strategy. Representative section with volume V_0 is further subdivided into subsections of volume V_m.

First a representative volume V_0 is selected, that gives sufficiently accurate estimates of $\left\langle \left\{ H_0^{(i)}(l) \right\} \right\rangle_V$. This volume is further divided into sub-sections of volume V_m such that $V_0/V_m = n$ and $n \in \mathbb{N}$. Using linearity of integration and substituting V_0 with nV_m one can write

$$H_v \approx \frac{\alpha}{nV_m} \sum_{i=1}^{V/V_0} \left(\sum_{j=1}^{V_0/V_m} \int_{V_m^{(ij)}} d\,(x,y,z) p_{\text{eff}}(x,y,z,l) dx dy dz \right). \tag{43}$$

Here $V_m^{(ij)}$ refers to i-th section and j-th sub-section of the partitioning scheme. Subsequently

$$H_v \approx \frac{\alpha}{V_m} \sum_{i=1}^{V/V_0} \left(\frac{1}{n} \sum_{j=1}^{n} \int_{V_m^{(ij)}} d\,(x,y,z) p_{\text{eff}}(x,y,z,l) dx dy dz \right), \tag{44}$$

which further leads to

$$H_v \approx \frac{\alpha}{V_m} \sum_{i=1}^{V/V_0} \left\langle \left\{ p_R^{(ij)}(l) \right\} \right\rangle_{V_{0i}}. \tag{45}$$

In the above equation the average is carried-out over the values of plastic reach, evaluated for each sub-section $V_m^{(ij)}$, and normalised by unit characteristic volume. Assembly of sub-sections forms V_{0i}. In the limit of relatively large n and small N, all averages will have approximately the same value *i.e.*

$$\left\langle \left\{ p_R^{(ij)}(l) \right\} \right\rangle_{V_{0i}} = \tilde{p}_R + \epsilon_i, \tag{46}$$

where $\left\langle \left\{ p_R^{(ij)}(l) \right\} \right\rangle$ is an estimator of $\tilde{p}_R$ and ϵ_i is associated bias. Noting that

$$\tilde{p}_R = \left\langle \left\{ p_R^{(ij)}(l) \right\} \right\rangle_{V_{0i}} - \epsilon_i, \tag{47}$$

one can write

$$H_v \approx \frac{\alpha}{V_m} \left\langle \left\{ p_R^{(ij)}(l) \right\} \right\rangle_{V_{0i}} \sum_{i=1}^{V/V_0} (1 - \epsilon_i) = \frac{V}{V_0} \frac{\alpha}{V_m} \left\langle \left\{ p_R^{(ij)}(l) \right\} \right\rangle_{V_{0i}} - \epsilon. \tag{48}$$

Quantity ϵ approximates the error of this simplification. Assuming that biases are normally distributed $\epsilon_i \sim \mathcal{N}(0, \sigma)$, using the expression for a sum of normally distributed random variables yields

$$\epsilon = \sum \sim \mathcal{N}\left(0, \frac{\alpha}{V_m}\frac{V}{V_0}\sigma\right). \tag{49}$$

This quantification of the numerical error holds only if differences between estimates are sufficiently small. Finally, all free parameters are assembled into one meta-parameter γ,

$$H_v = \frac{V}{V_0}\left\langle\left\{H_0^{(i)}(l)\right\}\right\rangle_V \approx \frac{V}{V_0}\frac{\alpha}{V_m}\left\langle\left\{p_R^{(ij)}(l)\right\}\right\rangle_{V_{0i}} = \gamma\langle p_R(l)\rangle, \tag{50}$$

where γ links estimate of plastic reach with cumulative hazard of a specimen, while α/V_m relates it to the average cumulative hazard.

Appendix D. Probability distributions and experimental data representation

Three common probability distributions are utilised to represent experimental galling data. The distributions, specified by their CDF (cumulative distribution function) F and cumulative hazard H, are as follows:

Exponential

$$F(x; x_0, \lambda) = \begin{cases} 1 - \exp\left(-\lambda(x - x_0)\right) & \geq x_0 \\ 0 & < x_0 \end{cases}, \tag{51}$$

$$H(x; x_0, \lambda) = \begin{cases} \lambda(x - x_0) & \geq x_0 \\ 0 & < x_0 \end{cases}, \tag{52}$$

log-normal

$$F(x; \mu, \sigma) = \begin{cases} \frac{1}{2} + \frac{1}{2}\mathrm{erf}\left(\frac{\ln x - \mu}{\sqrt{2}\sigma}\right) & x \geq 0 \\ 0 & x < 0 \end{cases}, \tag{53}$$

$$H(x; \mu, \sigma) = \begin{cases} \ln\left(\frac{1}{2} - \frac{1}{2}\mathrm{erf}\left(\frac{\ln x - \mu}{\sqrt{2}\sigma}\right)\right) & x \geq 0 \\ 0 & x < 0 \end{cases}, \tag{54}$$

Weibull

$$F(x; \lambda, k) = \begin{cases} 1 - \exp\left(-\left(\frac{x}{\lambda}\right)^k\right) & x \geq 0 \\ 0 & x < 0 \end{cases}. \tag{55}$$

$$H(x; \lambda, k) = \begin{cases} \left(\frac{x}{\lambda}\right)^k & x \geq 0 \\ 0 & x < 0 \end{cases}. \tag{56}$$

The sigmoid function introduced by Hummel *et al.* (2009) is not considered, as although it satisfies properties of a distribution, it allows predictions of non-zero galling probability for negative normal loads. Goodness of fit was tested using a least square method i.e. the objective function o defined as

$$o(\vec{\theta}) = \sum_{i=1}^{N}\left(F(x_i, \vec{\theta}) - y_i\right)^2 \tag{57}$$

where $\vec{\theta}$ are parameters of a given distribution and the pairs (x_i, y_i) represent experimental results. Optimal distribution parameters are ones that minimise the objective function. The results are presented in Figure D1.

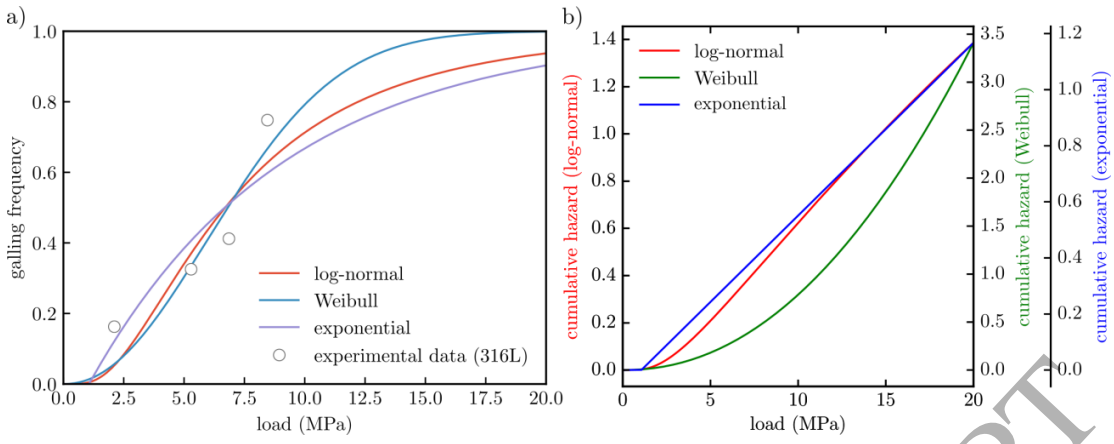

Figure D1. Illustration of the quantities evaluated from fitting distributions to experimental data. (a) Data points plotted against fitted distributions. (b) Resulting cumulative hazard. The values of the least-squares objective function, that quantifies goodness of the fit, were as follows: log-normal, $8.9 \cdot 10^{-3}$; Weibull, $5.2 \cdot 10^{-3}$; exponential, $1.3 \cdot 10^{-2}$.

Of the distribution function, the Weibull provides the best representation of the experimental data. On the other hand, data were provided without indication of measurement of uncertainty. Furthermore, the log-normal distribution resulted in a similar value of the objective function. Nevertheless, in this test, Weibull is considered as optimal. Model parameters were evaluated from three different sets of experimental data and the results are presented in Table C1.

type	scale parameter λ	shape parameter k	reference
316	14.5	1.74	(Harsha *et al.*, 2016)
316	9.14	3.31	(Hummel *et al.*, 2009)
316L	8.08	2.12	(Harsha *et al.*, 2016)
mean value	10.57	2.42	

Table C1. Parameters of Weibull distribution fitted to the experimental data.

Good agreement between exponent of the plastic reach (Figure 11 (e)) and exponents (shape parameters) in cumulative hazard of the Weibull distribution, will serve as a basis to postulate a relationship between them (equations (17) and (18)).

Appendix E. Analysis of repeatability

For the purpose of this study the framework has been slightly modified. From estimated parameters of the Weibull distribution, parameter γ was evaluated (equation (17)) and plastic reach scaled accordingly to obtain estimates of cumulative hazards H. Since plastic reach follows a power law only above l_0, and this is the point where it matches H of the Weibull distribution, the modified framework should provide slightly better estimates of the left tail. Furthermore, evaluated values of H were interpolated by fitting a relation

$$y(l) = ae^{\frac{b}{l}}\left(\frac{l}{c}\right)^{d}, \tag{58}$$

to corresponding results. In the above, a, b, c and d are free parameters, while l is the normal load. In this way a continuous approximation of $H(l)$ was obtained, allowing evaluation of galling frequency/probability F for any load within the considered range (see equation (18)). In consequence, for each l we have 6 potential predictions of $F(l)$, as each part of the three CPFE models was treated separately. However, l_0 and γ was evaluated by considering both parts of a given CPFE model. To quantify level of confidence associated with a single estimate we use standard methods of uncertainty analysis. Assuming that variations in estimates can be modelled by a random variable, an appropriate measure here is 95% confidence interval, defined as the range bounded by the 2.5$^{\text{th}}$ and 97.5$^{\text{th}}$ percentiles of the underlying distribution. However, finding the appropriate distribution to model the data is not always a trivial task. The recent standards (GUMS1, 2008) recommend to use the principle of maximum entropy (Jaynes, 1957) in combination with the method of moments. This translates to the most commonly used approach, where 1$^{\text{st}}$ and 2$^{\text{nd}}$ central moments, namely expected value μ and variance σ^2, are estimated by calculating sample mean m and standard deviation s, and matching $\mu \approx m$ and $\sigma^2 \approx s^2$. Given this available information, if the random variable is defined on the real line, the maximum entropy distribution is the normal distribution $\mathcal{N}(m, s^2)$. The 2.5$^{\text{th}}$ and 97.5$^{\text{th}}$ percentiles can be easily obtained from pre-calculated lookup tables. In the example considered, the 95%

confidence interval would be bounded by two values: $m - 1.96s$ and $m + 1.96s$. However, for random variables defined on the finite domain, and probability (frequency) is bounded to the interval [0,1] on a real line, so finding distribution that maximises entropy is not trivial. Furthermore, matching simple sample statistics with distribution parameters might be impossible. Therefore, it was decided to model the data using a distribution that fits best to the considered example. The assessed failure distribution represents fractions of samples that galled versus total number of tested samples. Commonly accepted (Sweeting, 2011) choice here is beta distribution with probability density defined as

$$p^{(\mathrm{Beta})}(x,\alpha,\beta) = \frac{\Gamma(\alpha+\beta)}{\Gamma(\alpha)\Gamma(\beta)} x^{\alpha-1}(1-x)^{\beta-1}, \tag{59}$$

where $x \in [0,1]$ and Γ is the gamma function. Parameters α and β are bounded to be non-negative. The procedure is as follows. For each value of load l_i $(i = 1,2,\dots,N)$ we evaluate six estimates of galling frequencies $F_{ij}(l_i)$ (j= 1,2,…,6) and calculate sample mean

$$m_i = \frac{1}{6}\sum_{j=1}^{6} F_{ij}(l_i) \tag{60}$$

and sample variance

$$s_i^2 = \frac{1}{6}\sum_{j=1}^{6} \left(F_{ij}(l_i) - m_i\right)^2. \tag{61}$$

Then corresponding estimates of the parameters are

$$\widehat{\alpha_\iota} = m_i\left(\frac{m_i(1-m_i)}{s_i^2} - 1\right), \tag{62}$$

and

$$\widehat{\beta_\iota} = (1-m_i)\left(\frac{m_i(1-m_i)}{s_i^2} - 1\right). \tag{63}$$

In other words, for each load l_i a different beta distribution is evaluated with densities $p_i^{(\mathrm{Beta})}\left(F_{l_i}, \widehat{\alpha_\iota}, \widehat{\beta_\iota}\right)$, where F_{l_i} is the corresponding galling frequency. In Figure 16, the 2.5, 50 and 97.5 percentiles of the beta distribution are calculated using functions from SciPy module for Python (Jones *et al.*, 2001).

References

ASTM G196, ASTM G196-08, Standard Test Method for Galling Resistance of Material Couples, ASTM International, West Conshohocken, PA, www.astm.org, 2016.

ASTM G98-02, 2002, ASTM G98-02, "Standard Test Method for Galling Resistance of Materials", ASTM International, West Conshohocken, PA, www.astm.org, 2002.

Able Electropolishing, Able Electropolishing, "Electropolishing Refines Surfaces Affected By Galling", http://blog.ableelectropolishing.com/electropolishing-refines-surfaces-affected-galling, Accessed: 21-08-2017

Agarwal 1990, S. C. Agarwal and H. Ocken, "The microstructure and galling wear of a laser-melted cobalt-base hardfacing alloy", Wear, vol. 140, no. 2, pp. 223-233, Nov. 1990.

Antony 1983, K. C. Antony, "Wear-Resistant Cobalt-Base Alloys", JOM J. Miner. Met. Mater. Soc., vol. 35, no. 2, pp. 52-60,. 1983.

Archard 1956, J. F. Archard and W. Hirst, "The Wear of Metals under Unlubricated Conditions", Proceedings of the Royal Society A: Mathematical, Physical and Engineering Sciences, 236(1206), pp. 397–410, 1956.

Atamert 1993, S. Atamert, J. Stekly, "Microstructure, Wear Resistance, and Stability of Cobalt Based and Alternative Iron Based Hardfacing Alloys", Surface Engineering, 9(3), pp. 231-240, 1993.

Bachmann 2010, F. Bachmann, R. Hielscher, and H. Schaeben, "Texture analysis with MTEX–free and open source software toolbox", Solid State Phenomena, vol. 160, Trans Tech Publications, 2010.

ACCEPTED MANUSCRIPT

Bhansali 1982, K. J. J. Bhansali and A. E. E. Miller, "The role of stacking fault energy on galling and wear behavior", Wear, vol. 75, no. 2, pp. 241-252, Jan. 1982

Blochwitz 2005, C. Blochwitz, W. Tirschler, "Twin boundaries as crack nucleation sites. Crystal Research and Technology", 40(1-2), pp. 32-41, 2005.

Boas 1977, M. Boas and A. Rosen, "Effect of load on the adhesive wear of steels", Wear, vol. 44, no. 2, pp. 213-222, Sep. 1977.

Boyer 1987, HE. Boyer, Atlas of Stress-strain Curves", ASM International, Metals Park, Ohio 44073, USA, 1987.

Buchely 2005, M. F. Buchely, J. C. Gutierrez, L. M. León, A. Toro, "The effect of microstructure on abrasive wear of hardfacing alloys", Wear, Vol. 259, pp. 52-61, 2005

Budinski 1981, K. G. Budinski, "Incipient galling of metals", Wear, vol. 74, no. 1, pp. 93-105, 1981.

Burwell 1952, J. T. Burwell and C. D. Strang, Metallic Wear. Proceedings of the Royal Society of London. Series A, Mathematical and Physical Sciences Mathematical and Physical Sciences, 212(1111), pp. 470-477, 1952.

Cao 2009, J. Cao, W. Zhuang, S. Wang, K. C. Ho , N. Zhang, J. Lin, T. A. Dean, "An integrated crystal plasticity FE system for microforming simulation", Journal of Multiscale Modelling, 1(01), pp. 107-124, 2009.

Choo 2000, S. Choo, C. K. Kim, K. Euh, S. Lee, J. Jung, S. Ahn, "Correlation of microstructure with the wear resistance and fracture toughness of hardfacing alloys reinforced with complex carbides", Metallurgical and Materials Transactions A, 31(December), pp. 3041-3052, 2000.

Cockeram 1997, B. V. Cockeram, R. F. Buck, and W. L. Wilson, "Laboratory galling tests of several commercial cobalt-free weld hardfacing alloys", Surf. Coatings Technol., vol. 9495, pp. 495-500, 1997.

Cockeram 2002, B. V Cockeram, "Some observations of the influence of δ-ferrite content on the hardness, galling resistance, and fracture toughness of selected commercially available iron-based hardfacing alloys", Metall. Mater. Trans. A, vol. 33, no. 11, pp. 3403-3419, 2002.

Dang 2013, V. Dang, J. Perret-Liaudet, J. Scheibert, J. A Bot, "Direct numerical simulation of the dynamics of sliding rough surfaces." Computational Mechanics, 52(5), pp. 1169–1183, 2013

Davis 1994, J. R. Davis, "Stainless steels", ASM international, 1994.

Delstar Metal Finishing, Delstar Metal Finishing, "Benefits of Electropolishing.", https://www.delstar.com/benefits-of-electropolishing, Accessed: 21-08-2017.

Dunne 2007, F. P. E. Dunne, D. Rugg, A. Walker, "Lengthscale-dependent, elastically anisotropic, physically-based hcp crystal plasticity: Application to cold-dwell fatigue in Ti alloys", International Journal of Plasticity, 23(6), pp. 1061-1083, 2007.

GUMS1, JCGM, "Evaluation of measurement data - Supplement 1 to the 'Guide to the expression of uncertainty in measurement' - Propagation of distributions using a Monte Carlo method", JCGM 101:2008, sec. 6.4, Bureau international des poids et mesures, 2008.

Gee 1969, A. W. J. de Gee, G. W. Rowe, (1969). "Glossary of Terms and Definitions in the Field of Friction", Wear and Lubrication Tribology. Organization for Economic Co-operation and Development, Paris.

Hornbogen 1975, E. Hornbogen, "The role of fracture toughness in the wear of metals", Wear, vol. 33, no. 2, pp. 251-259, 1975.

Hsu 1980, K. L. Hsu, T. M. Ahn, and D. A. Rigney, "Friction, wear and microstructure of unlubricated austenitic stainless steels", Wear, vol. 60, no. 1, pp. 13-37, 1980.

Hummel 2008, S. R. Hummel, "Development of a galling resistance test method with a uniform stress distribution", Tribol. Int., vol. 41, no. 3, pp. 175-180, 2008.

Hummel 2009, S. R. Hummel and J. Helm, "Galling50, a Stochastic Measure of Galling Resistance", J. Tribol., vol. 131, no. 3, 34502, 2009.

Jaynes 1957, E. T. Jaynes, "Information theory and statistical mechanics", Physical review, 106.4:620, 1957.

Jones 2001, E. Jones, T. Oliphant, P. Peterson et al., "SciPy: Open source scientific tools for Python", http://www.scipy.org/, 2001.

Kang 2010, G. Kang, Y. Dong, H. Wang, Y. Liu and X. Cheng, "Dislocation evolution in 316L stainless steel subjected to uniaxial ratchetting deformation", Materials Science and Engineering: A, 527(21), pp. 5952-5961, 2010.

Kim 2000, J. K. Kim and S. J. Kim, "The temperature dependence of the wear resistance of iron-base NOREM 02 hardfacing alloy", Wear, vol. 237, no. 2, pp. 217-222, 2000.

ACCEPTED MANUSCRIPT

Kim 2001, J. K. Kim, G. M. Kim, and S. J. Kim, "The effect of manganese on the strain-induced martensitic transformation and high temperature wear resistance of Fe-20Cr-1C-1Si hardfacing alloy", J. Nucl. Mater., vol. 289, no. 3, pp. 263-269, 2001.

Kragelsky 1976, I. V. Kragelsky and N. M. Alekseev, "On the Calculation of Seizure Considering the Plastic Flow of the Surficial Layers", J. Lubr. Technol., vol. 98, no. 1, pp. 133-138, Jan. 1976

Manonukul 2004, A. Manonukul and F. P. E. Dunne, High–and low–cycle fatigue crack initiation using polycrystal plasticity. In Proceedings of the Royal Society of London A: Mathematical, Physical and Engineering Sciences, volume 460, pp. 1881-1903. The Royal Society, 2004.

McCarthy 2014, Oliver J. McCarthy, J. P. McGarry and Sean B. Leen, Micro-mechanical modelling of fretting fatigue crack initiation and wear in Ti6Al4. International Journal of Fatigue, 62: pp. 180-193, 2014.

Ninham 1998, A. J. Ninham, A. V. Levy, "The erosion of carbide-metal composites", Wear, 121(3), pp. 347-361, 1998.

Ocken 1985, H. Ocken, "Reducing the Cobalt Inventory in Light Water Reactors", Nucl. Technol., vol. 68, no. 1, pp. 18-28, 1985.

Ocken 1995, H. Ocken, "The galling wear resistance of new iron-base hardfacing alloys: a comparison with established cobalt- and nickel-base alloys", Surface and Coatings Technology, 76–77(2), pp. 456-461, 1995.

Ohriner 1991, E. K. Ohriner, T. Wada, E. P. Whelan and H. Ocken, "The chemistry and structure of wear-resistant, iron-base hardfacing alloys", Metallurgical Transactions A, 22(5), pp. 983-991, 1991.

Olson 1976, G. B. Olson and M. Cohen, "A general mechanism of martensitic nucleation: Part I. General concepts and the FCC to HCP transformation", Metall. Trans. A, vol. 7, no. 12, pp. 1897-1904, Dec. 1976.

Harsha 2015, P. Harsha, P. K. Limaye, R. Tyagi, A. Gupta. "Development of Tribological Test Equipment and Measurement of Galling Resistance of Various Grades of Stainless Steel", Journal of Tribology, 138(2), p. 24501, 2015.

Persson 2003, D. H. E. Persson, S. Jacobson, and S. Hogmark, "Antigalling and low friction properties of a laser processed Co-based material", J. Laser Appl., vol. 15, no. 2, pp. 115-119, 2003.

Persson 2003-2, D. H. E. Persson, S. Jacobson, S. Hogmark, "Effect of temperature on friction and galling of laser processed Norem 02 and Stellite 21", Wear, 255(16), pp. 498-503, 2003.

Podgornik 2004, B. Podgornik, S. Hogmark, O. Sandberg. "Influence of surface roughness and coating type on the galling properties of coated forming tool steel." Surface and Coatings Technology 184.2-3, pp. 338-348, 2004.

Podgornik 2012, B. Podgornik, J. Jerina, "Surface topography effect on galling resistance of coated and uncoated tool steel" Surface and Coatings Technology, 206(11–12), pp. 2792–2800, 2012

Quey 2011, R. Quey, P. R. Dawson, F. Barbe, "Large-scale 3D random polycrystals for the finite element method: Generation, meshing and remeshing", Computer Methods in Applied Mechanics and Engineering, 200(17), pp. 1729-1745, 2011.

Rabinowicz 1961, E. Rabinowicz, "Influence of Surface Energy on Friction and Wear Phenomena", J. Appl. Phys., vol. 32, no. 8, pp. 1440-1444, 1961.

Rabinowicz 1973, E. Rabinowicz, "Friction seizure and galling seizure", Wear, vol. 25, pp. 357-363, 1973.

Schumacher 1981, W. Schumacher, "Wear of Materials", American Society of Mechanical Engineers, New York, 1981.

Suh 1973, P. N. Suh, "The delamination theory of wear", Wear, vol. 25, no. 1, pp. 111-124, 1973.

Sweeting 2011, P. Sweeting, "Statistical distributions. In Financial Enterprise Risk Management, International Series on Actuarial Science", pp. 134-220, Cambridge, Cambridge University Press, 2011.

Vikström 1994, J. Vikström, "Galling resistance of hardfacing alloys replacing Stellite," Wear, vol. 179, no. 12, pp. 143-146, 1994.

Vinogradov 1957, I. E. Vinogradov, "The significance of frictional seizure", Razvit. Teor. Treniya i Iznashivaniya (Developments Theory Frict. Wear), pp. 65-73, 1957.

Waite 2006, R. A. Waite, S. R. Hummel, A. Herr, and G. Dalton, "Analysis of the stress field in a threshold-galling test", Tribol. Int., vol. 39, no. 11, pp. 1421-1427, 2006.

Weibull 1939, W. Weibull, "A statistical theory of the strength of materials", Proc. Roy. Swed. Inst. Eng. Res, p. 151, 1939.

Weyler 2012, R. Weyler, J. Oliver, T. Sain, J.C. Cante, On the contact domain method: A comparison of penalty and Lagrange multiplier implementations. Computer Methods in Applied Mechanics and Engineering, 205–208(1), pp. 68–82. 2012

ACCEPTED MANUSCRIPT

Yang 1985, Z. Y. Yang, M. G. S. Naylor, D. A. Rigney, “Sliding wear of 304 and 310 stainless steels”, Wear, vol. 105, no. 1, pp. 73-86, 1985.

Zhang 2011, P. Zhang, D. Balint, J. Lin., “Controlled Poisson Voronoi tessellation for virtual grain structure generation: a statistical evaluation”, Philosophical Magazine 91.36, pp. 4555-4573, 2011.

Zok 2017, F. W. Zok, “On weakest link theory and Weibull statistics”, Journal of the American Ceramic Society, 100(4), pp. 1265-1268, 2017.

ACCEPTED MANUSCRIPT